
Research Articles: Neurobiology of Disease

Loss of Christianson Syndrome Na⁺/H + Exchanger 6 (*NHE6*) Causes Abnormal Endosome Maturation and Trafficking Underlying Lysosome Dysfunction in Neurons

<https://doi.org/10.1523/JNEUROSCI.1244-20.2021>

Cite as: J. Neurosci 2021; 10.1523/JNEUROSCI.1244-20.2021

Received: 18 May 2020

Revised: 5 July 2021

Accepted: 7 August 2021

This Early Release article has been peer-reviewed and accepted, but has not been through the composition and copyediting processes. The final version may differ slightly in style or formatting and will contain links to any extended data.

Alerts: Sign up at www.jneurosci.org/alerts to receive customized email alerts when the fully formatted version of this article is published.

Copyright © 2021 Pescosolido et al.

This is an open-access article distributed under the terms of the Creative Commons Attribution 4.0 International license, which permits unrestricted use, distribution and reproduction in any medium provided that the original work is properly attributed.

Journal of Neuroscience: Research Article (Neurobiology of Disease)

Number of Pages: 59

Number of Words-Abstract: 243

Number of Words-Significance Statement: 120

Number of Words-Introduction: 579

Number of Words-Discussion: 1,557

Number of Figures: 13

Number of Tables: 0

Number of Movies: 1

Loss of Christianson Syndrome Na⁺/H⁺ Exchanger 6 (NHE6) Causes Abnormal Endosome Maturation and Trafficking Underlying Lysosome Dysfunction in Neurons

Matthew F. Pescosolido PhD^{1,2}, Qing Ouyang PhD^{1,2}, Judy S. Liu MD PhD^{1,3},
and Eric M. Morrow MD PhD^{1,2#}

¹Department of Molecular Biology, Cell Biology and Biochemistry; and Carney Institute for Brain Science, Brown University, Laboratories for Molecular Medicine, 70 Ship Street, Providence, RI;

²Center for Translational Neuroscience, Carney Institute for Brain Science and Brown Institute for Translational Science, Brown University, 70 Ship Street, Providence, RI;

³Department of Neurology, Rhode Island Hospital, 593 Eddy Street, Providence, RI

#To whom correspondence should be addressed:

Eric M. Morrow MD PhD

Brown University, Lab for Molecular Medicine,

70 Ship Street, Providence, RI 02912

Tel: 401-863-9778

Fax: 401- 432-1607

E-mail: eric_morrow@brown.edu

Abbreviated Title: Loss of NHE6 Causes Abnormal Endosome Maturation

CONFLICT OF INTEREST STATEMENT

The authors declare no competing financial interests.

ACKNOWLEDGEMENTS

This work was supported by the National Institutes of Health grants R01NS113141,

R01MH102418, R01MH105442, and R21MH115392 (to EMM). MFP was supported by

National Institutes of Health National Research Service Award (F31NS093880) and an

advanced predoctoral training grant (T32NS062443, PI:Lipscombe/Moore). We thank D.

M. Pegtel for kindly providing the CD63-pHluorin construct.

48 **ABSTRACT**

49 Loss-of-function mutations in endosomal Na⁺/H⁺ exchanger 6 (NHE6) cause the X-linked
50 neurologic disorder Christianson syndrome (CS). Patients exhibit symptoms associated
51 with both neurodevelopmental and neurodegenerative abnormalities. While loss of
52 NHE6 has been shown to over-acidify the endosome lumen, and is associated with
53 endolysosome neuropathology, NHE6-mediated mechanisms in endosome trafficking
54 and lysosome function have been understudied. Here, we show that NHE6-null mouse
55 neurons demonstrate worsening lysosome function with time in culture, likely as a result
56 of defective endosome trafficking. NHE6-null neurons exhibit overall reduced lysosomal
57 proteolysis despite over-acidification of the endosome and lysosome lumen. Akin to
58 Nhx1 mutants in *Saccharomyces cerevisiae*, we observe decreased endosome-
59 lysosome fusion in NHE6-null neurons. Also, we find premature activation of pH-
60 dependent cathepsin D (CatD) in endosomes. While active CatD is increased in
61 endosomes, CatD activation and CatD protein levels are reduced in the lysosome.
62 Protein levels of another mannose 6-phosphate receptor (M6PR)-dependent enzyme, b-
63 N-acetylglucosaminidase, were also decreased in lysosomes of NHE6-null neurons.
64 M6PRs accumulate in late endosomes, suggesting defective M6PR recycling and
65 retromer function in NHE6-null neurons. Finally, coincident with decreased endosome-
66 lysosome fusion, using total internal reflection fluorescence (TIRF), we also find a
67 prominent increase in fusion between endosomal multivesicular bodies (MVBs) and the
68 plasma membrane (PM), indicating enhanced exosome secretion from NHE6-null
69 neurons. In summary, in addition to over-acidification of endosomes and lysosomes, loss
70 of NHE6 leads to defects in endosome maturation and trafficking, including enhanced
71 exosome release, contributing to lysosome deficiency and potentially leading to
72 neurodegenerative disease.

73 **SIGNIFICANCE STATEMENT**

74 Loss-of-function mutations in the endosomal Na⁺/H⁺ exchanger 6 (NHE6) cause
75 Christianson syndrome (CS), an X-linked neurological disorder. Loss of NHE6 has been
76 shown to over-acidify endosomes; however, endosome trafficking mechanisms have
77 been understudied, and the mechanisms leading to neurodegeneration are largely
78 unknown. In NHE6-null mouse neurons *in vitro*, we find worsening lysosome function
79 with days in culture. Notably, pH-dependent lysosome enzymes, such as cathepsin D
80 (CatD), have reduced activity in lysosomes yet increased, precocious activity in
81 endosomes in NHE6-null neurons. Further, endosomes show reduced fusion to
82 lysosomes, and increased fusion to the plasma membrane with increased exosome
83 release. This study identifies new mechanisms involving defective endosome maturation
84 and trafficking that impair lysosome function in CS, likely contributing to
85 neurodegeneration.

86 **INTRODUCTION**

87 The nervous system is vulnerable to endolysosome dysfunction. Lysosomal
 88 storage disorders (LSDs), which are caused by mutations in lysosome-associated
 89 genes, provide primary evidence linking endolysosomal dysfunction with neurologic
 90 disease (Platt et al., 2012; Boustany, 2013). Additional genetic studies have further
 91 implicated endolysosomal genes in more common neurodegenerative diseases such as
 92 Alzheimer's disease (AD) and Parkinson's disease (PD) (Fraldi et al., 2016; Sharma et
 93 al., 2018; Winckler et al., 2018; Lie and Nixon, 2019).

94 The process of endosome maturation involves the transition of endosomes in the
 95 earlier stages of the endocytic pathway to the degradative route, thereby ensuring
 96 proper trafficking of cargo assigned for degradation to the lysosome (Huotari and
 97 Helenius, 2011; Scott et al., 2014). Progressive acidification of the endolysosomal lumen
 98 from early to late stages of the endocytic pathway is a key feature of endosome
 99 maturation, and regulated by a number of membrane-based ion channels, pumps, and
 100 transporters (Mellman et al., 1986; Casey et al., 2010; Huotari and Helenius, 2011).
 101 Endosomal Na^+/H^+ exchangers (NHEs) (namely NHE6 and NHE9) represent a class of
 102 cation exchangers that are thought to alkalinize intra-luminal pH by exchanging luminal
 103 H^+ for cytosolic cations (e.g. Na^+ or K^+). NHE6 protein has been shown to be particularly
 104 abundant on early and recycling endosomes (>80%) (Brett et al., 2002; Ohgaki et al.,
 105 2010; Ouyang et al., 2013), and is also on late endosomes (approximately 50%) at least
 106 in neurons (Ouyang et al., 2013).

107 Exemplifying the importance of endosomal NHEs to human brain function, loss-
 108 of-function mutations in X-linked *NHE6* cause the neurologic disorder Christianson
 109 syndrome (CS) (Gilfillan et al., 2008; Pescosolido et al., 2014). Affected males present
 110 with intellectual disability, epilepsy, ataxia, and postnatal microcephaly (Pescosolido et
 111 al., 2014). Neurodegenerative features identified in CS patients include cerebellar

112 degeneration and widespread neuronal loss and gliosis, potentially involving tau
 113 deposition (Garbern et al., 2010; Pescosolido et al., 2014); however, the cellular
 114 mechanisms mediating neurodegenerative pathology in CS remain unclear. Ouyang et
 115 al. (2013) found that loss of NHE6 in neurons led to an overacidification of the
 116 endosomal lumen, consistent with a critical role for NHE6 in the regulation of luminal pH
 117 during endosome maturation. The functions of NHE6 in endosome maturation and
 118 trafficking are less well understood. Abnormalities in these primary endosome processes
 119 may secondarily lead to defects in lysosome function. Neuropathological features seen
 120 in lysosome disorders have been previously reported in the CS mouse model (Stromme
 121 et al., 2011; Sikora et al., 2016); however, the molecular mechanisms underlying
 122 potential lysosome deficiency in CS are unknown.

123 In this study, we investigate mechanisms of endolysosome dysfunction in NHE6-
 124 null neurons. We show here that loss of NHE6 in primary neurons *in vitro* causes
 125 worsening lysosome function with days in cultures, and that this lysosome deficiency is
 126 associated with defects in endosome maturation and trafficking. NHE6-null neurons
 127 exhibit overall reduced lysosomal proteolysis, despite overacidification of the endosome
 128 and lysosome lumen. Akin to Nhx1 mutants in *Saccharomyces cerevisiae*, the yeast
 129 homolog of NHE6 (Karim and Brett, 2018), we observe decreased endosome-lysosome
 130 fusion in NHE6-null neurons. We find precocious activation of the pH-dependent
 131 lysosome enzyme cathepsin D (CatD) in endosomes, with evidence of reduced CatD
 132 trafficked to lysosomes. While loss of NHE6 inhibits endosome-lysosome fusion, we find
 133 greater fusion between late endosomes/multivesicular bodies (MVBs) with the plasma
 134 membrane (PM), leading to enhanced exosome release. Overall, these novel disease
 135 mechanisms in CS, involving defective endosome maturation likely causing lysosome
 136 deficiency, place CS within the context of a growing category of neurodegenerative
 137 disorders with endolysosome dysfunction.

138

139 **MATERIALS AND METHODS**140 ***Materials***

141 Protease inhibitor (Roche, 05892970001), phosSTOP (Roche, 04906837001), PMSF
 142 (Sigma, 93482), Fluoromount-G (SouthernBiotech), Lipofectamine 2000 (Invitrogen,
 143 Cat#11668019), 22 mm poly-D-lysine-coated coverslips (Neuvitro, GG-22-1.5-PDL),
 144 black CellCarrier-96 Ultra microplates (PerkinElmer). The following compounds were
 145 used: 4-methyl-umbelliferyl-N-acetyl-b-D-glucosaminide (Millipore Sigma, 474502),
 146 Bafilomycin A1 (Sigma, B1793), DMSO (Sigma, D8418), Ionomycin (Sigma, I9657),
 147 NH₄Cl (Sigma, A9434), U18666A (Sigma, U3633). The following items were purchased
 148 through ThermoFisher Scientific: Alexa Fluor 546-transferrin (T23364), Alexa Fluor 594-
 149 BSA (A13101), Alexa Fluor 594-dextran (D22913), Alexa Fluor 647-dextran (D22914),
 150 B27 (17504044), BODIPY FL-pepstatin A (P12271), DQ-BSA (Green, D12050), FITC-
 151 transferrin (T2871), GlutaMAX (35050061), Oregon Green 488-dextran (D7171),
 152 ProLong Gold antifade mountant with DAPI (P36931), Tetramethylrhodamine-dextran
 153 (D1817).

154

155 ***Antibodies***

156 The following antibodies were used for western blot: Actin (Sigma, A3853, Ms, 1:1000),
 157 Cathepsin D (R&D Systems, AF1029, Gt, 1:1000), CD63 (Abcam, EPR21151-ab217345,
 158 Rb, 1:1000), ci-M6PR (Cell Signaling Technology, 14364S, Rb, 1:500), GAPDH (Sigma,
 159 G8795, Ms, 1:40000), LAMP1 (DSHB, 1D4B, Rt, 1:1000), RAB5 (Cell Signaling
 160 Technology, 3547, Rb, 1:1000), RAB7 (Sigma, R8779, Ms, 1:1000). The following
 161 antibodies were used for immunocytochemistry experiments: ci-M6PR (Abcam, 2G11-
 162 ab2733, Ms, 1:1000), Hoechst-33342 (ThermoFisher Scientific, H1399, 1:1600), LAMP1
 163 (Abcam, ab24170, Rb, 1:500 for BODIPY-Pepstatin A, 1:1000 for M6PR), LBPA

164 (Echelon Biosciences, Ms, 1:100), MAP2 (Abcam, ab5392, Ch, 1:5000), RAB5 (Cell
 165 Signaling Technology, 3547, Rb, 1:500), RAB7 (Abcam, ab137029, Rb, 1:100 for
 166 BODIPY-Pepstatin A, 1:500 for M6PR and 3D imaging), and TGN46 (Abcam, ab16059,
 167 Rb, 1:1000). The following secondary antibodies were used at a 1:800 dilution: anti-
 168 mouse Alexa Fluor 488, anti-chicken Alexa Fluor 594, anti-rabbit Alexa Fluor 594, anti-
 169 mouse Alexa Fluor 647, anti-rabbit Alexa Fluor 647, anti-rat Alexa Fluor 647.

170

171 ***Animals***

172 All animal care and use were performed in accordance with NIH guidelines and was
 173 approved under a protocol by the Brown University Institutional Animal Care and Use
 174 Committee.

175

176 ***Dissociated Hippocampal Cultures***

177 Dissociated hippocampal neurons were derived from mouse pups at P0-P1 as
 178 previously described (Ouyang et al., 2013). Cells were typically seeded at densities of
 179 either 3.0×10^5 /mL (immunocytochemistry) or 3.5×10^5 /mL (immunoblot and enzyme
 180 assays) unless otherwise specified. All treatments were added to Neurobasal media
 181 supplemented with B27 (2%), and glutamax (1%) unless otherwise specified. Cultured
 182 neurons were transfected at DIV 13 with Lipofectamine 2000 (Invitrogen, Carlsbad, CA).

183

184 ***Western Blot***

185 Western blots were analyzed by the Odyssey Clx Infrared Imaging System (LI-COR) and
 186 Odyssey software v5.2.5. Primary hippocampal neurons were washed with cold 1xPBS
 187 and lysed with RIPA buffer supplemented with 1% protease inhibitor on ice. Cultures
 188 were then scraped, put on ice for 1 hour and centrifuged for 10 minutes at 13,000 RPM
 189 at 4°C. Mouse hippocampal tissue was harvested at 8-weeks, lysed with tissue lysis

190 buffer (RIPA buffer supplemented with 1% protease inhibitor, 1% phosSTOP and 1%
 191 PMSF), homogenized, and put on ice for 1 hour. Brain tissue samples were then
 192 centrifuged for 15 minutes at 13,200 RPM at 4°C. Protein quantity was quantified for all
 193 samples using a BCA protein assay. Primary hippocampal cultures (5 or 10 µg) or
 194 hippocampal tissue (30 µg) were resolved on NuPAGE 4-12% SDS-polyacrylamide gels
 195 (Invitrogen). All proteins of interest were normalized to loading control proteins (e.g. actin
 196 or GAPDH). Western blot images have been cropped for presentation.

197

198 ***Lysosomal Enzyme Assays***

199 Enzyme activity was measured in 8-week old mouse brain tissue (e.g. hippocampus,
 200 cerebellum and cortex) and 14 DIV hippocampal neuronal cultures. b-N-
 201 Acetylglucosaminidase (B-NAG) activity was measured using the substrate 4-
 202 Nitrophenyl N-acetyl-b-D-glucosaminide (NP-GlcNAc) according to the kit protocol
 203 (Sigma, CS0780). Acid phosphatase activity was measured using the substrate 4-
 204 Nitrophenyl Phosphate according the kit protocol (Sigma, CS0740). Hippocampal
 205 primary culture (10 µg) or mouse brain tissue (20 µg) were incubated in triplicate for 10
 206 minutes at 37°C. Absorbance was measured at 405 nm on a Cytation3 microplate
 207 reader (BioTek) using Gen5 software v2.07.

208

209 ***Lysosome-Enriched Fractionation***

210 Lysosomes from the cortex and hippocampus of 4-month-old male Nhe6^{-f/y} and WT
 211 littermate mice were enriched using the lysosome isolation kit (LYSISO1, Sigma). The
 212 modified protocol from Bagh et al. (2017) was used. Briefly, brain tissue was
 213 homogenized in 4 volumes of 1x extraction buffer with protease inhibitor and spun for 10
 214 minutes at 1,000 g at 4°C. The supernatant was then centrifuged for 20 minutes at

215 20,000 g at 4°C. The crude lysosome fraction (CLF) pellet was resuspended in 1x
 216 extraction buffer and added to the 19% Optiprep gradient. The following Optiprep
 217 gradients were layered: 27%, 22.5%, 19% (including CLF), 16%, 12%, and 8%. Samples
 218 were ultracentrifuged (Optima MAX-XP, Beckman Coulter) for 4 hours at 150,000 g at
 219 4°C. Five fractions were collected at the junction of each gradient. Fractions 2 (12-16%)
 220 and 3 (16-19%), which had the highest LAMP1 protein levels, were combined and used
 221 for analysis. The same amount of protein was loaded for western blot (2.5 µg). Proteins
 222 of interest were normalized to LAMP1.

223

224 ***Confocal Microscopy***

225 Confocal z-stacks for the following experiments were acquired using an LSM 800 (Zeiss)
 226 microscope: (1) DQ-BSA, (2) AF-594 BSA, and (3) BODIPY-pepstatin A (from Figure 2)
 227 experiments. Images were collected using an oil-immersion 63x objective with
 228 1,024x1,024-pixel resolution. To ensure an unbiased selection, all neurons were
 229 selected using the DIC channel. For colocalization experiments (e.g. BODIPY-pepstatin
 230 A and M6PR), z-stack images were acquired using an Olympus FV3000 (Olympus)
 231 microscope. Images were collected using an oil-immersion 63x objective with 512x512-
 232 pixel resolution. pH and endosome-lysosome fusion experiments were imaged using the
 233 Opera Phenix High-Content Screening System (PerkinElmer). Single-plane (pH) or Z-
 234 stacks (endosome-lysosome fusion) images were collected with a water-immersion 63x
 235 objective. Endosome-lysosome fusion experiments were imaged using the Olympus
 236 FV3000 microscope. Z-stack images were collected using an oil-immersion 60x
 237 objective. For each experiment, laser settings were the same across all time points. For
 238 live-imaging, cells were placed in a humidity chamber and maintained at 37°C with 5%
 239 CO₂.

240

241 ***DQ-BSA Degradation***

242 Mouse hippocampal neuronal cultures were analyzed at DIV 3, 5, and 14. Cells were
243 treated with 20 µg/mL of DQ-BSA at 37°C. Cells were incubated with DQ-BSA for 30
244 minutes, washed twice with 1xPBS and chased for 1.5 hours with supplemented
245 Neurobasal media. Following DQ-BSA treatment, neurons were briefly rinsed with
246 1xPBS and fixed with 4% PFA for 10 minutes at RT. Cells were the washed with 1xPBS
247 3 times for 5 minutes each, with the first and second washes containing Hoechst. Slides
248 were mounted with Fluoromount-G.

249

250 ***BSA Uptake***

251 Mouse hippocampal neuronal cultures were analyzed at DIV 3, 5, and 14. Cells were
252 treated with 20 µg/mL of BSA conjugated with Alexa Fluor 594 (BSA-AF594) at 37°C.
253 Cells were incubated with BSA-AF594 for 30 minutes, briefly rinsed twice with 1xPBS,
254 and fixed with 4% PFA for 10 minutes at RT. Cells were then washed with 1xPBS 3
255 times for 5 minutes each, with the first and second washes containing Hoechst. Slides
256 were mounted with Fluoromount-G.

257

258 ***Active Cathepsin D Labeling Using BODIPY FL-pepstatin A***

259 Mouse hippocampal neuronal cultures were analyzed at DIV 3, 5, and 14. Cells were
260 treated with 1 µg/mL of BODIPY FL-pepstatin A for 1 hour at 37°C. Following BODIPY
261 FL-pepstatin A treatment, neurons were briefly rinsed twice with 1xPBS and fixed with
262 4% PFA for 10 minutes at RT. Cells were then washed 3 times with 1xPBS for 5 minutes
263 each, with the first and second washes containing Hoechst. Slides were mounted with
264 Fluoromount-G.

265

266 ***Active Cathepsin D Colocalization with Endolysosomal Markers***

267 Mouse hippocampal neuronal cultures were analyzed at DIV 5 and 14 with the same
 268 BODIPY FL-pepstatin A treatment as the prior experiment. Following treatment, cells
 269 were washed 3 times with warm 1xPBS, fixed/permeabilized with 4% PFA in 1xPBS for
 270 30 minutes at RT, and washed 3 times with 1xPBS for 5 minutes per wash. For dextran
 271 experiments, cells were then mounted with Fluoromount-G. For non-dextran
 272 experiments, cells were then blocked with 10% goat serum in 1xPBS and 0.1% TritonX-
 273 100 or 0.01% saponin (LBPA) for 1 hour at RT. Cells were then incubated with primary
 274 antibodies overnight in 1xPBS and 0.1% TritonX-100 or 0.01% saponin (LBPA) at 4°C.
 275 The next day cells were washed twice with 1xPBS, incubated with secondary antibodies
 276 in 1xPBS and 0.1% TritonX-100 or 0.01% saponin (LBPA) for 1 hour at RT, washed
 277 once with 1xPBS, and mounted with Fluoromount-G. For dextran experiments, cells
 278 were incubated with 5 mg/mL dextran (1:25) for 3 hours at 37°C at DIV 4 or 13. Cells
 279 were washed twice with 1xPBS and chased overnight (~16 hours) with Neurobasal
 280 media.

281

282 ***Endosome and Lysosome pH***

283 Mouse hippocampal neuronal cultures were analyzed at DIV 8. For each animal, 3-4
 284 wells were seeded in CellCarrier-96 Ultra microplates (PerkinElmer) for replication
 285 purposes. Lysosome pH was measured using a protocol adapted from Johnson et al.
 286 (2016). At DIV 7, cells were incubated with 0.1 mg/mL each of Oregon green 488-
 287 dextran (OG-dextran) and tetramethylrhodamine-dextran (TMR-dextran) for 2 hours at
 288 37°C. They were washed 3 times with 1xPBS and then chased overnight in
 289 supplemented Neurobasal media. Prior to live-imaging, cells were incubated with

290 Hoechst-33342 (1:1600) in supplemented Neurobasal media-minus phenol red for 10
291 minutes to label cell nuclei. They were then washed once with 1xPBS and imaged with
292 supplemented Neurobasal media-minus phenol red. The fluorescence ratio was
293 converted to absolute pH using a pH calibration curve. The calibration curve was
294 generated by imaging pH standards (e.g. 3.5, 4.5, and 5.5) in a calibration solution (125
295 mM KCl, 25 mM NaCl, 10 μ M monensin, 25 mM MES, and adjusted to a final pH using
296 1N NaOH or 1N HCl). For bafilomycin A1 experiments, 100 nM were added with
297 Hoechst-33342 in supplemented Neurobasal media-minus phenol red for 10 minutes.
298 Cells were then imaged in supplemented Neurobasal media-minus phenol red with 100
299 nM of bafilomycin A1. Endosome pH was measured in primary hippocampal neurons at
300 DIV 5 as previously described (Ouyang et al., 2019).

301

302 ***Endosome-Lysosome Fusion***

303 Cells were seeded on CellCarrier-96 Ultra microplates (PerkinElmer). Mouse
304 hippocampal neuronal cultures were analyzed at DIV 5. At DIV 4, cells were incubated
305 with 0.25 mg/mL of TMR-dextran for 2 hours at 37°C. Cells were then washed twice with
306 1xPBS and chased overnight with supplemented Neurobasal media. At DIV 5, cells were
307 incubated with 0.5 mg/mL Alexa Fluor 647-dextran and Hoechst-33342 (1:5000) for 10
308 minutes at 37°C, washed twice with 1xPBS, and imaged immediately with supplemented
309 Neurobasal media-minus phenol red. For bafilomycin A experiments, cells were treated
310 with 100 nM bafilomycin A1 while incubating with Alexa Fluor 647-dextran and Hoechst-
311 33342. Live-cell imaging was performed using the Opera Phenix High-Content
312 Screening System in supplemented Neurobasal media-minus phenol red. Z-stack
313 images were taken every 20 minutes over the span of 2 hours (i.e. 7 time points).

314

315 ***Total Internal Reflection Fluorescence (TIRF) Microscopy***

316 Exosome secretion events were visualized by ring-TIRF using the DeltaVision OMX SR
 317 imaging system (GE). Mouse hippocampal neuronal cultures were analyzed at 14 DIV.
 318 Cells were plated on 22 mm poly-D-lysine-coated coverslips (Neuvitro, Vancouver, WA)
 319 at 3.5×10^5 /mL density. At 13 DIV, cells were co-transfected with CD63-pHluorin and
 320 empty-mCherry plasmids using Lipofectamine 2000. Prior to imaging, neurons were
 321 transferred to Tyrode's solution (124 mM NaCl, 3 mM KCl, 2 mM CaCl_2 , 1 mM MgCl_2 , 10
 322 mM HEPES pH=7.4, 5 mM D-glucose). Images were collected on a 63x TIRF objective
 323 at 1024x1024 resolution with oil 1.522. To visualize transfected cell location, a widefield,
 324 single-plane image was collected prior to TIRF imaging. Laser settings were identical
 325 across all experiments. Environmental settings were constant for O_2 (20%), CO_2 (5%),
 326 and humidity (50%). Five-minute videos were collected per cell at 2 Hz (i.e. every 500
 327 ms). Cultured neurons were treated with bafilomycin A1 (100 nM for 2 hours) and
 328 U18666A (1.5 ug/mL for 16 hours) (Strauss et al., 2010).

329
 330 ***Image Acquisition and Analysis***

331 For lysosome pH experiments, twenty images were collected per well for each sample.
 332 Data was collected from at least 3 independent experiments using at least 4 animals per
 333 genotype. Image analysis was performed using Harmony software (version 4.9, Perkin
 334 Elmer). The DAPI channel was used to define the nucleus and cell soma regions using
 335 the "Find Nuclei" and "Find Cytoplasm" building blocks, respectively. Cell count was
 336 calculated from identified nuclei. Live cells were then distinguished using a minimum
 337 nuclear area threshold. Dextran-labelled lysosomes were identified using the "Find
 338 Spots" building block. Spots (i.e. lysosomes) that met inclusion criteria for fluorescence
 339 intensity and size (15-140 pixels²) were included for analysis. Fluorescence intensity for
 340 both OG- and TMR-dextran channels was measured per spot. Spots within the "Find

341 Nuclei" building block were classified as soma while all other spots were classified as
 342 processes. To determine lysosome pH, the ratio of OG-dextran fluorescence intensity to
 343 TMR-dextran fluorescence intensity was calculated. A calibration curve was generated
 344 by plotting the values of the OG-dextran/TMR-dextran ratio against the pH values
 345 obtained from the pH standards for each experiment. Fluorescent intensity values
 346 collected from experimental samples were converted to pH values using the calibration
 347 curve formula. Endosome pH analysis was performed as previously described (Ouyang
 348 et al., 2019).

349 For active CatD labeling experiments, 20 images were selected for each sample.
 350 Data was collected from at least 4 independent experiments using at least 4 different
 351 mouse litters. Sample file names were randomized to ensure unbiased analysis.
 352 BODIPY-Pepstatin A images were analyzed using ImageJ software (NIH). Prior to
 353 analysis, the same background subtraction was applied to all images (i.e. rolling ball
 354 radius 50 pixels). Puncta quantification was performed using the "Analyze Particles"
 355 function. The same image settings were applied to all images: subtract background (30),
 356 threshold (70). Mean fluorescence intensity (MFI) was calculated by outlining individual
 357 neurons in the DIC channel using the Freehand tool and measuring green channel
 358 fluorescence. A background measurement was collected using the Oval tool to draw an
 359 area size between 20-30. MFI was calculated as: mean intensity - background.

360 For active CatD colocalization experiments, 10 images were selected for each
 361 sample. Data was collected from at least 3 independent experiments using at least 3
 362 different mouse litters. A single-plane image was selected, cropped, and channels were
 363 separated in ImageJ. The following thresholds were applied: MaxEntropy (BODIPY-
 364 pepstatin A), Intermodes (LAMP1, RAB7, LBPA, RAB5), and RenyiEntropy (dextran).
 365 Colocalization was calculated using the Manders' coefficient in JACoP (Bolte and
 366 Cordelieres, 2006). Analysis settings include: Confocal, Wavelength A=488, Wavelength

367 B=647 (LAMP1, RAB7, LBPA, RAB5) or 568 (dextran), NA=1.4, refractive index=1.518.
 368 Calibration settings were selected using "Get calib. From ImgA", which reported the
 369 following values: xy calib=96.57 and z calibration=1000.

370 M6PR colocalization experiment parameters were nearly identical to active
 371 cathepsin D colocalization experiments (see above). The following thresholds were
 372 applied: MaxEntropy (M6PR, TGN46, RAB7), Moments (LAMP1), and Intermodes
 373 (RAB5). Analysis settings include: Confocal, Wavelength A=488 (M6PR), Wavelength
 374 B=647 (all other markers).

375 For endosome-lysosome fusion experiments, Z-stacks from the same 6 regions
 376 of interest were collected for each sample across all time points. Data was collected
 377 from 5 independent experiments using 7 animals per genotype. Image analysis was
 378 performed using Harmony software (version 4.9) similar to lysosome pH experiments.
 379 The DAPI channel was used to define the nucleus using the "Find Nuclei" building
 380 blocks. Cell count was calculated from identified nuclei. Live cells were then
 381 distinguished using a minimum nuclear area threshold. Dextran-labelled vesicles were
 382 identified using the "Find Spots" building block. Spots (i.e. TMR-dextran and Alexa Fluor
 383 647-dextran) that met inclusion criteria for fluorescence intensity were included for
 384 analysis. Percent of fusion events (i.e. Alexa Fluor 647-dextran + TMR-dextran
 385 spots/Total Alexa Fluor 647-dextran spots) were analyzed using "Find Population"
 386 building blocks with Alexa Fluor 647-dextran as population1 and TMR-dextran as
 387 population 2. Fusion event data are expressed as % fold change to time point 0 for each
 388 animal.

389 3D-reconstruction analysis was performed using Imaris 5.1 software (Bitplane).
 390 Z-stack confocal images were cropped and volume was reconstructed – surface and
 391 "MIP" (i.e. maximum intensity projection). File names were randomized to ensure
 392 unbiased analysis. Puncta were manually thresholded by adjusting: (1) background

393 subtraction, (2) absolute intensity, and (3) Split touching Objects. To segment the
 394 nucleus, the DAPI marker was manually traced throughout the entire z-stack. The
 395 distance between different markers was calculated using the “Distance Transformation”
 396 module, with “Outside SurfaceObject” selected.

398 ***Lysosome Exocytosis Experiments***

399 Media was collected from mouse primary hippocampal cultures at DIV 14. Approximately
 400 8×10^5 cells were added to a well of a 6-well plate. For each sample, primary cultures
 401 were seeded in duplicate to allow for treatment comparisons. Neurons were treated with
 402 either ionomycin (10 μ m) or DMSO for 10 minutes at 37°C. Media was then collected
 403 and centrifuged for 10 minutes at 13,200 at 4°C to pellet any cellular debris.

404 b-Hexosaminidase (b-Hex) activity was measured using a protocol adapted from
 405 Laulagnier et al. (2011) and using the Tyrode’s solution previously mentioned. Following
 406 media collection, cells were washed 1x with cold 1xPBS and lysed with 500 μ l of cell
 407 lysis buffer (RIPA buffer + 1% protease inhibitor). Cells were put on ice for 15 minutes,
 408 spun for 10 minutes at 13,200 RPM at 4°C, and the supernatant was collected. For
 409 media and cell lysate samples, 50 μ l were added to a 96-well in triplicate. In each well,
 410 the following were added: 5 μ l of lysine, 16 μ l of reaction mixture (1 mM 4-methyl-
 411 umbellyferyl-N-acetyl-b-D-glucosaminide in 11.2 mM citrate, 17.6 mM Na_2HPO_4 ,
 412 pH=4.5), and 45 μ l of 1xPBS. Samples were incubated for 30 minutes at 37°C, followed
 413 by the addition of 100 μ l of stop reaction (2M Na_2CO_3 , 1.1M glycine, pH=10.2).
 414 Fluorescence was measured at Ex/Em = 365/450 nm on a Cytation3 microplate reader
 415 (BioTek) using Gen5 software v2.07. b-Hex activity was calculated by averaging each
 416 sample and subtracting the control sample average (i.e. Tyrode’s solution without any

primary neurons). Released activity was calculated using the following formula: (media – control media)/(cell lysis – cell lysis buffer) x 100.

Cathepsin D activity was measured using the synthetic substrate GKPIFFRLK(Dnp)-D-R-NH₂ according to the kit protocol (Abcam, ab65302). Culture media was aspirated at 14 DIV and replaced with 1 mL of Tyrode's solution (124 mM NaCl, 3 mM KCl, 2 mM CaCl₂, 1 mM MgCl₂, 10 mM HEPES pH=7.4, 5 mM D-glucose) prior to treatment. A total of 50 ul of sample media was added per well in duplicate and incubated for 1.5 hours at 37°C. Fluorescence was measured at Ex/Em = 328/460 nm on a Cytation3 microplate reader (BioTek) using Gen5 software v2.07. Enzyme activity was calculated by subtracting the media-only average from each sample average.

LDH was measured and calculated according to the protocol (Sigma, MAK066). For each sample, 50 ul of media was added to a 96-well plate in duplicate. Absorbance was measured at 450 nm on a Cytation3 microplate reader (BioTek) using Gen5 software v2.07.

Statistical Analysis

Data is presented as means ± SEM. The *n* represents the number of biological replicates for each experiment. For microscopy experiments, the *n* typically represents the number of cells, although it may also represent the number of animals (e.g. pH and endosome-lysosome fusion experiments) analyzed. Most statistical analyses were performed using GraphPad Prism version 7. Normality was assessed using the D'Agostino and Pearson omnibus normality test. For experiments with a low sample size (*n*<7) where D'Agostino and Pearson omnibus normality test was unable to be tested, Gaussian distribution was assumed. Unless otherwise specified, two group comparisons were analyzed by unpaired, two-tailed Student's *t* test (data normally-distributed) or

442 Mann-Whitney *U* test (data not normally-distributed). For data not normally-distributed
 443 with distribution shapes between the 2 groups, a log10 transformation was applied and a
 444 normality test was performed on the transformed data. Effect size was calculated using
 445 Cohen's *d* (sample size $n > 20$), Hedges's *g* (samples size $n < 20$), or Glass's delta (if
 446 standard deviation significantly different). Linear mixed model analysis was performed
 447 using SPSS version 25. Endosome-lysosome fusion experiments were analyzed using a
 448 linear mixed model, with % endosome-lysosome fusion as the dependent variable.
 449 Genotype and time points were factors, while litter was entered as a covariate. Intercept,
 450 genotype, time, litter, and time x genotype were modeled as fixed effects, while animal
 451 was modeled as a random effect. Time points (e.g. 20, 40, 60, 80, 100, and 120) were
 452 calculated as % endosome-lysosome fusion normalized to time point 0. The time x
 453 genotype interaction for % endosome-lysosome fusion was the primary outcome
 454 variable. Analysis of exosome secretion following various treatments was analyzed using
 455 Kruskal-Wallis test with Dunn's test for multiple comparisons. An ordinal logistic
 456 regression was performed using Stata SE (release 15). The number of MVB-PM
 457 fusion/exosome release events (i.e. counts) were considered ordered categorical
 458 variables. Lysosomal exocytosis experiments were performed with two-way ANOVA
 459 followed by Tukey's multiple comparisons test when necessary.

460

461

462 **RESULTS**

463 ***Loss of NHE6 Leads to Reduced Lysosomal Protease Function***

464 To examine the relationship between loss of NHE6 and lysosome functioning, we
 465 investigated the degradative capacity of primary hippocampal neurons *in vitro*. We
 466 treated NHE6-null and wild-type (WT) male neurons with DQ-BSA (i.e. bovine serum
 467 albumin conjugated with fluorophores that emit only upon degradation) to measure

468 proteolysis of endocytosed material (Vazquez and Colombo, 2009). We first examined
 469 DQ-BSA puncta features using 3D-reconstruction of primary hippocampal neurons at 5
 470 DIV (Figure 1A). This time point was chosen as some of the earliest overacidified
 471 endosomes findings in NHE6-null neurons were observed at 5 DIV (Ouyang et al.,
 472 2013). NHE6-null neurons had significantly fewer DQ-BSA puncta (Figure 1B), smaller
 473 average individual punctum size (Figure 1C), and less total summed puncta volume per
 474 cell (Figure 1D) compared to WT neurons. There were no differences in DQ-BSA
 475 distribution across the cell, as measured by distance from the nucleus (Figure 1E). To
 476 further investigate lysosome degradation, we measured the mean fluorescence intensity
 477 (MFI) of DQ-BSA treated neurons across a range of *in vitro* time points that reflect key
 478 neuronal processes such as axonal outgrowth (3 DIV), dendritic outgrowth (5 DIV), and
 479 synaptic maturation (14 DIV) (Dotti et al., 1988; Craig and Banker, 1994). NHE6-null
 480 neurons displayed significantly decreased proteolytic activity across all 3 timepoints
 481 compared to WT littermate controls, with worsening dysfunction at older timepoints.
 482 Effect size by Cohen's D was 0.23 as compared to 0.64 at 3 DIV and 14 DIV
 483 respectively (Figures 1F and 1G). Importantly, this decrease in degradative signal was
 484 not due to differences in BSA internalization (Figures 1H and 1I). These results indicate
 485 that loss of NHE6 leads to worsening lysosomal protease activity with time *in vitro*
 486 relative to control.

487

488 ***NHE6-Null Neurons Have Reduced Overall Cathepsin D Activity***

489 Hydrolases perform the degradative function of lysosomes and their activity is
 490 dependent upon the highly acidic lysosomal lumen (Braulke and Bonifacino, 2009).
 491 Lysosomal enzyme dysfunction represents a shared mechanism across many
 492 neurological disorders leading to the accumulation of macromolecules in cells

493 (Boustany, 2013; Lloyd-Evans and Haslett, 2016; Mazzulli et al., 2016). Based on our
 494 observations of deficient lysosomal protease function in NHE6-null neurons, we next
 495 examined the function of specific lysosome enzymes. To examine lysosome enzyme
 496 functioning, we analyzed the aspartic protease cathepsin D whose dysfunction has been
 497 reported across multiple neurodegenerative disorders (Vidoni et al., 2016).

498 To measure active cathepsin D, we treated male Nhe6^{-/-} and wildtype littermate
 499 primary hippocampal neurons with BODIPY FL pepstatin A. For this probe, the CatD-
 500 specific inhibitor pepstatin A has been conjugated with a pH-insensitive fluorophore
 501 (Chen et al., 2000). NHE6-null neurons demonstrated significantly reduced active CatD
 502 activity at DIV 5 and 14 (Figure 2A). Specifically, NHE6-null neurons had significantly
 503 decreased signal intensity (Figure 2B) and fewer puncta (Figure 2C), both worsening
 504 with days in culture. There were no differences in puncta size (data not shown). We
 505 investigated whether these CatD findings extended to mouse brain tissue. Therefore, we
 506 quantified active CatD protein levels biochemically in male Nhe6^{-/-} and WT littermate
 507 hippocampus at 8-weeks-old. Cleaved-CatD (i.e. the enzymatically active form) was
 508 significantly decreased in Nhe6^{-/-} mice (large effect size, Hedges's $g=1.77$) (Figure 2D
 509 and 2E).

510 To determine whether other lysosomal enzymes are affected, we measured the
 511 activity of b-N-Acetylglucosaminidase (B-NAG) and acid phosphatase in NHE6 mouse
 512 brain tissue (e.g. cerebellum, cortex, and hippocampus) from acutely dissected brains at
 513 8-week-old, as well as from primary hippocampal neurons at 14 DIV. B-NAG activity was
 514 significantly reduced in male NHE6-null hippocampal tissue as well as primary
 515 hippocampal cultures compared to male WT littermates [large effect size, Hedges's
 516 $g=0.78$ (tissue) and Hedges's $g=1.42$ (cultures)] (Figure 2F). No differences were found
 517 in the cortex or cerebellum. There were no differences in acid phosphatase activity
 518 across all brain tissue regions and primary hippocampal neurons at 14 DIV (Figure 2G).

519 These findings may reflect differences in lysosomal enzyme trafficking routes. Many
 520 newly synthesized lysosomal enzymes are transported from the trans-Golgi network
 521 (TGN) to the endocytic pathway by binding to mannose 6-phosphate receptors (M6PR),
 522 including CatD and B-NAG (von Figura and Hasilik, 1986; Ghosh et al., 2003). There is
 523 evidence to support the notion that acid phosphatase is trafficked via a distinct, M6PR-
 524 independent pathway (Braun et al., 1989; Peters et al., 1990). Taken together, these
 525 results indicate that loss of NHE6 leads to deficits *ex vivo* and *in vitro* in cathepsin D and
 526 B-NAG function, with both enzymes being trafficked in a M6PR-dependent manner.

527

528 ***Reduced Lysosome Intra-Luminal pH in NHE6-Null Neurons***

529 Given loss of NHE6 leads to hyper-acidification of the endosome lumen *in vitro* (Ouyang
 530 et al., 2013), we sought to determine whether intra-luminal pH in lysosomes was also
 531 affected. We adapted a ratiometric fluorescence microscopy protocol using dextran from
 532 Johnson et al. (2016) to measure the luminal pH of lysosomes. Primary hippocampal
 533 neurons were treated with both pH-sensitive (i.e. Oregon green 488) and pH-insensitive
 534 (i.e. tetramethylrhodamine) dextran and chased overnight to allow for trafficking to
 535 lysosomes (Figure 3A). The fluorescence ratio was converted to absolute pH using a pH
 536 calibration curve. Using a high-content imaging system, we found that NHE6-null
 537 neurons had significantly lower intra-lysosomal pH compared to WT male neurons
 538 (Figure 3B). Specifically, both the soma and processes contained more acidic lysosomes
 539 in NHE6-null neurons. Primary hippocampal neurons were treated with bafilomycin A1,
 540 as a positive control, to alkalinize the luminal pH of lysosomes (Figure 3C). As expected,
 541 lysosomal pH increased and there were no significant differences between NHE6-null
 542 and WT neurons (Figure 3D). To further verify our prior results on intra-endosomal pH in
 543 NHE6 null cells, but now utilizing our high-content imaging system, we examined
 544 transferrin-positive early/recycling endosome pH using fluorescent ratio imaging (Figure

3E). NHE6-null neurons had significantly lower endosome pH in both the soma and processes (Figure 3F). These results corroborate our previously published findings that NHE6-null neurons display lower intra-endosomal (Ouyang et al., 2013); however here, we extend our studies to demonstrate a more acidic pH in the lumen of lysosomes in the absence of NHE6.

NHE6-Null Neurons Have Abnormal Active Cathepsin D Distribution Across Endosome and Lysosome Compartments

Cathepsin D is trafficked to lysosomes in various enzymatically-inactive forms from the Golgi complex to endosomes until reaching the highly acidic lysosomal lumen where it is converted to its active form in a pH-dependent fashion (Zaidi et al., 2008). CatD is generally trafficked by the mannose 6-phosphate receptor (M6PR) pathway (von Figura and Hasilik, 1986), although M6PR-independent routes have been reported (Gopalakrishnan et al., 2004; Canuel et al., 2008). Since NHE6-null primary neurons exhibit deficiencies in the enzymatically-active CatD, we investigated if this was due to impaired trafficking and/or distribution of CatD in the endosome and lysosome compartment. Given our prior data demonstrating over-acidification of endosomal pH in NHE6-null neurons, we hypothesized that CatD may undergo precocious pH-dependent activation.

We measured the subcellular distribution of active CatD using BODIPY FL pepstatin A with different endosome and lysosome markers. To reliably label lysosomes, primary hippocampal neurons were treated with fluorescent dextran and chased overnight. NHE6-null neurons exhibited significantly less active CatD-dextran colocalization compared to WT littermate controls at DIV 5 and 14 (Figure 4A and 4B). This result reflects less active CatD in lysosome compartments in NHE6-null neurons, with increasing effect size with days in culture. We do not believe this apparent reduction

571 in colocalization is due to alterations in the size or distribution of lysosome compartment
 572 alone. Using 3D volumetric reconstruction of dextran puncta, we observed no
 573 differences at 5 DIV (Figure 5), a time at which we see decreases in colocalization of the
 574 mutant. We also found reduced active CatD colocalization using another lysosome-
 575 associated marker LAMP1 whereby NHE6-null neurons showed decreased active CatD-
 576 LAMP1 colocalization at DIV 5 and 14, again with increasing effect size with time in
 577 culture (Figure 4C and 4D). However, we are aware that LAMP1 labels both degradative
 578 lysosomes as well as non-degradative organelles of endosomal and autophagic origin
 579 (Gowrishankar et al., 2015; Cheng et al., 2018; Kulkarni and Maday, 2018; Yap et al.,
 580 2018). Again, we do not believe that this pattern of active CatD is caused solely by
 581 alterations in lysosome size or distribution. There were no differences in LAMP1 protein
 582 levels in the mutant (Figure 6A and 6B). 3D volumetric reconstruction revealed that
 583 NHE6-null neurons had significantly more LAMP1 puncta and total LAMP1 volume at 5
 584 DIV (Figure 6C and 6D). However, we observed significantly fewer LAMP1 puncta and
 585 greater average LAMP1 puncta volume at 14 DIV (Figure 6E and 6F).

586 By contrast to the findings of reduced active CatD in mutant lysosomes, NHE6-
 587 null neurons displayed significantly greater colocalization of active CatD within the early
 588 and late endosome compartment. The late endolysosome compartment was initially
 589 studied using the marker RAB7 at DIV 5 and 14, wherein there was more active CatD
 590 (Figure 4E and 4F). There were no differences in RAB7 protein levels yet NHE6-null
 591 neurons had larger RAB7 puncta volume and more total RAB7 volume at DIV 5 (Figure
 592 7). We examined active CatD colocalization with lysobisphosphatidic acid (LBPA), an
 593 atypical phospholipid found on the internal membrane of late endosomes (Kobayashi et
 594 al., 1998). Active CatD was colocalization with LBPA was enhanced at DIV 5 relative to
 595 control, and although not statistically-significant, showed greater colocalization at DIV 14
 596 (Figure 4G and 4H). Also, NHE6-null neurons exhibited significantly greater active CatD

colocalization with the early endosome marker RAB5, at DIV 5 but not DIV 14 (Figure 4I and 4J). There were no differences in RAB5 protein levels or puncta features in mutant neurons (Figure 8). These endosome results are consistent with over-acidification of the endosome lumen (Figure 3E and 3F) and precocious activation of CatD; however, perhaps with a compensatory response in the early endosome by later stages of culturing.

Our data support a reduced level and/or activity of CatD in the lysosome, suggesting that loss of NHE6 impairs CatD trafficking to lysosomes. To further corroborate our lysosome findings, we measured CatD protein levels directly within the lysosome by cellular fractionation using lysosome-enriched fractions (LEF) collected *ex vivo* from 4-month old CS mouse hippocampal and neocortical tissue combined. LEFs from NHE6-null mice had significantly decreased pro- and cleaved-CatD levels compared to male littermate controls (Figure 4K and 4L). These results show strong effective sizes (Hedges's $g=1.26$ for pro-CatD and Hedges's $g=1.99$ for cleaved). Collectively, these findings indicate that loss of NHE6 causes two important effects on CatD: first, premature cathepsin D activity in earlier stages in the endocytic pathway; and second, impaired trafficking of cathepsin D to lysosomes.

Loss of NHE6 Alters Mannose 6-Phosphate Receptor (M6PR) Distribution

Given our findings that M6PR-dependent lysosomal enzymes (namely CatD and B-NAG) are notably affected in NHE6 null neurons, we investigated whether this was due, in part, to impaired trafficking of M6PRs. M6PR shuttles between the trans-Golgi network and the endocytic pathway (Brown et al., 1986; Hirst et al., 1998; Ghosh et al., 2003; Lin et al., 2004; Kucera et al., 2016). Prior to reaching lysosomes, M6PRs are retrogradely transported back to the TGN via the retromer complex (e.g. VPS26, VPS29, and VPS35) (Arighi et al., 2004; Seaman, 2004; Cui et al., 2019). Notably, we did not

623 observe differences in M6PR protein levels by western blot between NHE6 null and
 624 control neurons (Figure 9A and 9B); however, NHE6-null neurons had significantly
 625 greater M6PR puncta numbers and total volume per cell at 14 DIV (Figure 9E and 9F).

626 To investigate the steady-state distribution of endogenous cation-independent-
 627 M6PR (CI-M6PR), we measured M6PR colocalization with markers for the TGN and
 628 endolysosome compartments. NHE6-null primary hippocampal neurons exhibited
 629 significantly decreased M6PR colocalization with the TGN marker TGN46 at DIV 5 and
 630 14 (Figure 10A and 10B). On the other hand, NHE6-null neurons showed significantly
 631 greater M6PR-RAB7 colocalization at DIV 5 and 14, reflecting enhanced distribution of
 632 M6PRs in the LE in NHE6-null neurons (Figure 10C and 10D). Furthermore, NHE6-null
 633 neurons demonstrated significantly greater M6PR-LAMP1 colocalization at DIV 5 and 14
 634 (Figure 10E and 10F). NHE6-null neurons also had significantly greater M6PR-RAB5
 635 colocalization at DIV 5, but not DIV 14 (Figure 10G and 10H). Taken together, these
 636 findings are consistent altered M6PR trafficking in NHE6-null neurons, perhaps reflecting
 637 defects in retrograde trafficking of M6PR back to Golgi.

638

639 ***NHE6-Null Neurons Have Diminished Endosome-Lysosome Fusion***

640 Loss of Nhx1 in *Saccharomyces cerevisiae*, the NHE6 homolog in yeast, impairs
 641 MVB fusion with vacuoles (i.e. the lysosome equivalent in yeast) (Karim and Brett,
 642 2018). Given these observations and our data on reduced CatD activity in lysosomes in
 643 neurons, we set out to measure endosome-lysosome fusion in primary hippocampal
 644 neurons. Primary neurons were incubated with TMR-dextran on DIV 4 to allow for
 645 trafficking to lysosomes. On DIV 5, cells were briefly incubated with Alexa Fluor 647-
 646 dextran for 10 minutes for internalization via endocytosis. Time-lapse images collected
 647 every 20 minutes over the span of 2 hours captured endosome-lysosome fusion events,
 648 as defined by endocytosed Alexa Fluor 647-dextran puncta that colocalized with the

649 lysosome marker TMR-dextran. NHE6-null neurons displayed significantly less
 650 endosome-lysosome fusion across all time points throughout a 2-hour span compared to
 651 WT littermate (Figure 11A and 11B). There was a statistically significant time x genotype
 652 interaction ($F [6, 72.0] = 3.432, p = 0.005$) (Figure 11B). As a control, cells were treated
 653 with bafilomycin A which disrupts the trafficking of late endosomes to lysosomes (van
 654 Weert et al., 1995). As expected, bafilomycin A treatment impaired endosome-lysosome
 655 fusion in WT and NHE6-null neurons. The kinetics of endosome-lysosome fusion
 656 between NHE6-null neurons without bafilomycin A and control neurons with bafilomycin
 657 A were similar. Our data therefore suggest that loss of NHE6 significantly impedes or
 658 delays endosome-lysosome fusion in neurons *in vitro*.

659

660 ***Loss of NHE6 Enhances MVB-PM Fusion and Exosome Secretion***

661 Given impaired endosome to lysosome trafficking, we investigated whether loss
 662 of NHE6 altered the trafficking of late endosomes/MVBs. We utilized a CD63-pHluorin
 663 construct to visualize MVB fusion with the plasma membrane (PM) in live neurons using
 664 total internal reflection fluorescence (TIRF) microscopy (Verweij et al., 2018; Bebelman
 665 et al., 2019). This construct is also able to visualize exosomes, a class of extracellular
 666 vesicles originating from endosomes (Colombo et al., 2014). Interestingly, endosomal
 667 acidification has been identified as a key regulator of exosome release (Parolini et al.,
 668 2009; Bonsergent and Lavieu, 2019; Bonsergent et al., 2021). In this experiment,
 669 individual MVB-PM fusion/exosome secretion events were scored in primary
 670 hippocampal neurons at 14 DIV (Figure 12A, and Movie 1). To reliably identify neurons
 671 transfected with the CD63-pHluorin, we co-transfected an mCherry vector to label
 672 neurons. Control neurons demonstrated a remarkably low level of MVB-PM fusion
 673 events; however, notably, NHE6-null neurons displayed significantly greater MVB-PM
 674 fusion/exosome secretion events compared to wildtype male littermate controls (Figure

12B). Statistical analysis using an ordinal logistic regression revealed NHE6-null neurons were more likely to exhibit multiple MVB-PM fusion/exosome secretion events (i.e. ≥ 2 events) than control neurons (Odds Ratio= 11.4; 95% CI=1.9, 66.6; $p=0.007$). As a positive control, we treated primary hippocampal neurons with bafilomycin A1 (Villarroya-Beltri et al., 2016) and U186668 (Strauss et al., 2010), each of which increase small-medium sized EV (smEV) secretion. Bafilomycin A1 treatment significantly increased MVB-PM fusion/exosome secretion in WT neurons compared to untreated neurons ($H(2)=12.44$, $p=0.002$, Kruskal-Wallis test with Dunn's test for multiple comparisons) (Figure 12C). In NHE6-null neurons, bafilomycin A1 treatment did not increase MVB-PM fusion/exosome secretion above untreated mutant neurons, possibly due to the high fusion events at baseline. We also measured CD63 protein levels in primary hippocampal neurons at 14 DIV. Interestingly, there was significantly less CD63 in NHE6-null neurons (Figure 12D and 12E). Taken together, these findings suggest that NHE6-null neurons display enhanced MVB-PM fusion and CD63-associated exosome secretion. Furthermore, it is unlikely that this reflects an increase in CD63 protein levels as CD63 protein levels were reduced in NHE6-null neurons, perhaps in part due to excess release of CD63-positive exosomes.

We also investigated whether loss of NHE6 also led to greater lysosome fusion with the plasma membrane, a Ca^{2+} -dependent process known as lysosomal exocytosis (Andrews, 2000; Blott and Griffiths, 2002). Enhancing lysosomal exocytosis has been shown to promote the extracellular release of pathogenic substrates in various lysosomal storage diseases (Medina et al., 2011). To measure lysosomal exocytosis *in vitro*, we measured the activity of extracellularly secreted lysosome enzymes in primary hippocampal neurons at DIV 14. As a positive control, cells were treated with ionomycin, a calcium ionophore that increases cytoplasmic Ca^{2+} concentration, which enhances lysosomal exocytosis (Rodriguez et al., 1997). Importantly, there were no differences in

701 released activity of the lysosomal enzyme b-hexosaminidase (b-hex) at baseline (i.e.
702 DMSO) as well as following ionomycin treatment in NHE6-null neurons relative to control
703 neurons (Figure 12F). Similar results were found when measuring released cathepsin D
704 enzyme activity (Figure 12G). There were no differences in cell death, as measured by
705 released lactate dehydrogenase (LDH) enzyme activity, across all treatments (Figure
706 12H). We therefore conclude that loss of NHE6 causes specific changes in MVB-PM
707 fusion/CD63-positive exosome release that does not extend to lysosomal exocytosis.

708

709 **DISCUSSION**

710 Loss-of-function mutations of the endosomal protein NHE6 cause Christianson
711 syndrome, an X-linked disorder characterized by severe neurodevelopmental as well as
712 neurodegenerative pathology (Gilfillan et al., 2008; Garbern et al., 2010; Pescosolido et
713 al., 2014). Loss of NHE6 has previously been shown to hyper-acidify endosomal
714 compartments and alter endosomal signaling in neurons (Ouyang et al., 2013;
715 Kucharava et al., 2020). However, we currently lack a comprehensive understanding of
716 how the endolysosomal pathway is affected in NHE6-null neurons. In this study, we
717 found that loss of NHE6 in primary hippocampal neurons leads to worsening lysosome
718 functioning with days in culture, likely due to impaired endosome maturation and
719 trafficking (Figure 13). We present evidence of precocious activation of pH-dependent
720 proteases, such as CatD, in endosomes, with reduced delivery of CatD to lysosomes
721 due to reduced endosome-lysosome fusion. We also present evidence of accumulation
722 of M6PR in late endosome, potentially reflecting defective retromer function. Coincident
723 with these late endosome trafficking defects, we find enhanced fusion of late endosomes
724 or MVB with the plasma membrane and enhanced exosome release in NHE6-null
725 neurons.

Neuropathological findings indicative of lysosome deficiency have been reported in a CS mouse model (Stromme et al., 2011; Sikora et al., 2016). These *in vivo* results are important as they strengthen the significance of our mechanistic studies here, indicating that our studies are not strictly attributable to the *in vitro* setting. In Stromme et al. (2011), NHE6-null mice exhibit features consistent with lysosomal storage diseases, such as pathologic accumulation of GM2 ganglioside and unesterified cholesterol in late endosomes and lysosomes that affect particular brain regions, including the hippocampus. In the current study we directly measured lysosomal degradation of endocytosed cargo *in vitro*. NHE6-null neurons displayed significantly less overall DQ-BSA fluorescence, indicating reduced overall degradative capacity, consistent with lysosome deficiency. Furthermore, it is unlikely that this difference in BSA degradation is due to less BSA being internalized in NHE6-null neurons, as we observed equivalent endocytosis of fluorescent BSA. Importantly, we observed worsening lysosome function in NHE6-null neurons with time in culture, suggesting that these defects may be secondary to endosomal trafficking defects accumulated over time.

We examined specific lysosome enzymes, including Cathepsin D, a pH-dependent aspartic lysosomal hydrolase. CatD gene mutations have been identified in the lysosomal storage disease neuronal ceroid-lipofuscinosis (NCL) subtype 10 (CLN10) (Siintola et al., 2006; Steinfeld et al., 2006). We found that loss of NHE6 leads to decreased mature, enzymatically-active cathepsin D both *in vitro* and *ex vivo* in NHE6-null tissue. NHE6-null neurons demonstrated overall decreased active CatD fluorescence and number of puncta, as measured by BODIPY-pepstatin A. A limitation to our imaging experiments is that while this probe is routinely used to visualize active CatD, pepstatin A is an aspartic protease inhibitor (Marciniszyn et al., 1976). Therefore, we cannot exclude that other aspartic proteases (e.g. cathepsin E, BACE1, etc.) are also labelled. However, our *ex vivo* experiments further support our interpretation that loss of

752 NHE6 leads to decreased active CatD specifically. We found decreased mature CatD
753 protein levels in 8-week-old NHE6-null hippocampal tissue compared to WT male
754 littermates by western blotting.

755 We also observed a unique endolysosomal distribution of active CatD in NHE6-
756 null neurons, consistent with precocious activation of CatD in endosomes. Notably,
757 acidification-dependent dissociation of M6PR-ligand complexes occur at a lower pH
758 (~5.8) than other ligands such as insulin, consistent with dissociation in late endosome
759 compartments (Borden et al., 1990); therefore, it may be possible that some level of
760 CatD may be mislocalized due to premature dissociations from M6PR. Furthermore,
761 previously (Ouyang et al., 2013; Kucharava et al., 2020), may be in part due to
762 premature dissociation of ligand and/or enhanced protease degradation of ligand-
763 receptor complexes within endosomes. Importantly and in contrast, we observe less
764 colocalization of active CatD with lysosomal markers (e.g. dextran and LAMP1). Our
765 findings that active CatD was less likely to colocalize with lysosome-associated markers
766 in NHE6-null neurons were further corroborated by our analysis of lysosome-enriched
767 fractions (LEF) brain tissue. NHE6-null LEF samples contained significantly less protein
768 levels of both the enzymatically-inactive pro-form as well as the active cleaved-form.
769 These results, along with reduced endosome-lysosome fusion, suggest that CatD is not
770 properly trafficked to degradative lysosomes, which is a shared pathobiologic feature
771 across some LSDs (Futerman and van Meer, 2004; Platt et al., 2012; Platt et al., 2018).

772 NHE6 plays a role in regulating the luminal pH of the endocytic pathway. Loss of
773 NHE6 has been shown to over-acidify the endosomal lumen in neurons (Ouyang et al.,
774 2013). However, it was not known whether NHE6 was also involved in the regulation of
775 lysosomal pH. We found that NHE6-null neurons had a significantly lower pH compared
776 to WT male littermates. To our knowledge, the only other disease-associated finding of
777 lysosome hyper-acidification was reported in patient fibroblasts with a dominant, gain-of-

778 function mutation in the Cl⁻/H⁺ exchanger *CLCN7* (Nicoli et al., 2019). Interestingly, these
 779 patients exhibited overlapping neurologic features with CS including cerebellar atrophy.
 780 These lysosome hyper-acidification findings are in contrast to a number of mutations
 781 associated with neurological disease that impair lysosome acidification such as *PS1* and
 782 *CLN1* (Lee et al., 2010; Lee et al., 2015; Colacurcio and Nixon, 2016; Bagh et al., 2017).
 783 Our *in vitro* findings are suggestive of NHE6 contributing to lysosomal pH homeostasis.
 784 Interestingly, reduced lysosomal pH may occur as a result of proton diffusion from the
 785 endosome compartment. Prior literature indicates that NHE6 is not localized to
 786 lysosomes (Brett et al., 2002; Ohgaki et al., 2010).

787 Studies of impaired lysosome enzyme trafficking in NHE6-null neurons suggests
 788 impairment in M6PR-dependent trafficking. In our studies here, we find reduced CatD
 789 and B-NAG, both M6PR-dependent enzymes (von Figura and Hasilik, 1986; Ghosh et
 790 al., 2003), but not reduced acid phosphatase, a M6PR-independent enzyme (Braun et
 791 al., 1989; Peters et al., 1990), in lysosomes. In Stromme et al. (2011), they found
 792 reduced b-Hexosaminidase in hippocampus, a third M6PR-dependent enzyme (Hasilik
 793 and Neufeld, 1980). We observed that the steady-state distribution of M6PRs in NHE6-
 794 null neurons was skewed favoring greater colocalization with endolysosome markers,
 795 with strongest co-localization in late endosome, and less colocalization with the TGN,
 796 suggesting defective retrograde trafficking from endosomes to the TGN, possibly
 797 involving retromer function. A consequence of this perturbed trafficking of M6PRs is
 798 decreased replenishment of the endocytic pathway of lysosome enzymes. Since we
 799 found no differences in M6PR protein levels, it is unlikely that insufficient M6PR protein
 800 is being produced in NHE6-null mice. Future experiments may examine retromer defects
 801 in NHE6-null neurons more directly. Overall, our data are consistent with lysosome
 802 deficiency caused by impaired trafficking of M6PR-dependent enzymes to lysosome in
 803 NHE6-null neurons.

804 Late endosome fusion with the lysosome is a crucial step in the delivery of (1)
 805 newly synthesized lysosomal proteins and (2) endocytosed cargo for degradation (Luzio
 806 et al., 2007). Our findings support the conclusion that endosome-lysosome fusion is
 807 hampered in NHE6-null neurons *in vitro*. These results are consistent with a recent study
 808 of the yeast NHE6 ortholog, Nhx1, which shows that Nhx1 regulates multivesicular body
 809 (MVB) fusion with vacuoles (i.e. lysosome equivalent in yeast) (Karim and Brett, 2018).
 810 Currently, the specific molecular mechanisms for this fusion defect is not known. This
 811 could involve dysfunction of critical regulators of endosome-lysosome fusion such as the
 812 molecular fusion machinery (Ballabio and Bonifacino, 2019). Interesting, our data on
 813 accumulation of M6PR in Rab7 late endosomes suggests a second defect in late
 814 endosome trafficking, namely potentially involving retromer function. A unifying
 815 hypothesis might suggest that a defect in late endosome maturation may concurrently
 816 lead to these distinct defects in late endosome trafficking. Importantly, it is also unknown
 817 whether autophagosome-lysosome fusion is delayed in NHE6-null neurons. Taken
 818 together, our findings are consistent with loss of NHE6 impairing late endosome
 819 maturation, and specifically the ability of endosomes to fuse with lysosomes, which
 820 reflects important new mechanistic insight into disease pathophysiology.

821 Our data using a novel CD63-pHluorin construct (Verweij et al., 2018; Bebelman
 822 et al., 2019) provide further evidence of altered late endosome trafficking in NHE6-null
 823 mice. Specifically, NHE6-null neurons demonstrate enhanced MVB fusion with the
 824 plasma membrane along with CD63-associated exosome release. We observe a very
 825 low basal rate of CD63-associated exosome release in control neurons. Endolysosome
 826 dysfunction has been shown to enhance exosomal secretion (Strauss et al., 2010;
 827 Villarroya-Beltri et al., 2016; Gauthier et al., 2017) as well as proteins associated with
 828 neurodegenerative disorders (Alvarez-Erviti et al., 2011; Miranda et al., 2018). Cells with
 829 compromised lysosome function may increase exosome secretion as a protective

830 mechanism to bypass lysosomes and release endosomal cargo extracellularly (Levy,
831 2017; Miranda et al., 2018). While loss of NHE6 led to an upregulation in MVB/late
832 endosome fusion with the plasma membrane in neurons *in vitro*, there were no
833 differences lysosome fusion with the plasma membrane (i.e. lysosomal exocytosis).

834 In summary, our study provides insight into how endolysosome functioning is
835 perturbed by the loss of NHE6, underlying the pathophysiology of Christianson
836 syndrome. We show that loss of NHE6 impairs lysosome degradative function as well as
837 disrupts trafficking of endosomes to lysosomes. Interestingly, we observed NHE6-null
838 neurons exhibit impaired endosome-lysosome fusion while, simultaneously, enhanced
839 release of MVB-derived exosomes. CS may exemplify lysosome deficiency secondary to
840 defects in endosome maturation and trafficking, broadening the spectrum of lysosome-
841 related neurologic disorders. In conclusion, these studies indicate that in addition to
842 playing a role in regulation in intra-endosomal and lysosome pH, loss of NHE6 has
843 important impact on endosome maturation and trafficking.

844 **AUTHOR CONTRIBUTIONS**

845 MFP, QO, JSL, and EMM designed research; MFP, QO, JSL, and EMM performed
846 research; MFP, QO, JSL, and EMM analyzed data; MFP, QO, JSL, and EMM wrote the
847 paper. All authors approved the final version of the manuscript.

848

849 **REFERENCES**

- 850 Alvarez-Erviti L, Seow Y, Schapira AH, Gardiner C, Sargent IL, Wood MJ, Cooper JM
851 (2011) Lysosomal dysfunction increases exosome-mediated alpha-synuclein release
852 and transmission. *Neurobiology of disease* 42:360-367.
- 853 Andrews NW (2000) Regulated secretion of conventional lysosomes. *Trends in cell*
854 *biology* 10:316-321.
- 855 Arighi CN, Hartnell LM, Aguilar RC, Haft CR, Bonifacino JS (2004) Role of the
856 mammalian retromer in sorting of the cation-independent mannose 6-phosphate
857 receptor. *The Journal of cell biology* 165:123-133.
- 858 Bagh MB, Peng S, Chandra G, Zhang Z, Singh SP, Pattabiraman N, Liu A, Mukherjee
859 AB (2017) Misrouting of v-ATPase subunit V0a1 dysregulates lysosomal acidification in
860 a neurodegenerative lysosomal storage disease model. *Nature communications*
861 8:14612.
- 862 Ballabio A, Bonifacino JS (2019) Lysosomes as dynamic regulators of cell and
863 organismal homeostasis. *Nature reviews Molecular cell biology*.
- 864 Bebelman MP, Bun P, Huveneers S, van Niel G, Pegtel DM, Verweij FJ (2019) Real-
865 time imaging of multivesicular body-plasma membrane fusion to quantify exosome
866 release from single cells. *Nature protocols*.
- 867 Blott EJ, Griffiths GM (2002) Secretory lysosomes. *Nature reviews Molecular cell biology*
868 3:122-131.

- 869 Bolte S, Cordelieres FP (2006) A guided tour into subcellular colocalization analysis in
870 light microscopy. *Journal of microscopy* 224:213-232.
- 871 Bonsergent E, Lavieu G (2019) Content release of extracellular vesicles in a cell-free
872 extract. *FEBS letters* 593:1983-1992.
- 873 Bonsergent E, Grisard E, Buchrieser J, Schwartz O, Théry C, Lavieu G (2021)
874 Quantitative characterization of extracellular vesicle uptake and content delivery within
875 mammalian cells. *Nature communications* 12:1864.
- 876 Borden LA, Einstein R, Gabel CA, Maxfield FR (1990) Acidification-dependent
877 dissociation of endocytosed insulin precedes that of endocytosed proteins bearing the
878 mannose 6-phosphate recognition marker. *The Journal of biological chemistry* 265:8497-
879 8504.
- 880 Boustany RM (2013) Lysosomal storage diseases--the horizon expands. *Nature reviews*
881 *Neurology* 9:583-598.
- 882 Braulke T, Bonifacino JS (2009) Sorting of lysosomal proteins. *Biochimica et biophysica*
883 *acta* 1793:605-614.
- 884 Braun M, Waheed A, von Figura K (1989) Lysosomal acid phosphatase is transported to
885 lysosomes via the cell surface. *The EMBO journal* 8:3633-3640.

- 886 Brett CL, Wei Y, Donowitz M, Rao R (2002) Human Na(+)/H(+) exchanger isoform 6 is
 887 found in recycling endosomes of cells, not in mitochondria. *American journal of*
 888 *physiology Cell physiology* 282:C1031-1041.
- 889 Brown WJ, Goodhouse J, Farquhar MG (1986) Mannose-6-phosphate receptors for
 890 lysosomal enzymes cycle between the Golgi complex and endosomes. *The Journal of*
 891 *cell biology* 103:1235-1247.
- 892 Canuel M, Korkidakis A, Konnyu K, Morales CR (2008) Sortilin mediates the lysosomal
 893 targeting of cathepsins D and H. *Biochemical and biophysical research communications*
 894 373:292-297.
- 895 Casey JR, Grinstein S, Orlowski J (2010) Sensors and regulators of intracellular pH.
 896 *Nature reviews Molecular cell biology* 11:50-61.
- 897 Chen CS, Chen WN, Zhou M, Arttamangkul S, Haugland RP (2000) Probing the
 898 cathepsin D using a BODIPY FL-pepstatin A: applications in fluorescence polarization
 899 and microscopy. *Journal of biochemical and biophysical methods* 42:137-151.
- 900 Cheng XT, Xie YX, Zhou B, Huang N, Farfel-Becker T, Sheng ZH (2018)
 901 Characterization of LAMP1-labeled nondegradative lysosomal and endocytic
 902 compartments in neurons. *The Journal of cell biology*.
- 903 Colacurcio DJ, Nixon RA (2016) Disorders of lysosomal acidification-The emerging role
 904 of v-ATPase in aging and neurodegenerative disease. *Ageing research reviews* 32:75-
 905 88.

- 906 Colombo M, Raposo G, Thery C (2014) Biogenesis, secretion, and intercellular
 907 interactions of exosomes and other extracellular vesicles. Annual review of cell and
 908 developmental biology 30:255-289.
- 909 Craig AM, Banker G (1994) Neuronal polarity. Annual review of neuroscience 17:267-
 910 310.
- 911 Cui Y, Carosi JM, Yang Z, Ariotti N, Kerr MC, Parton RG, Sargeant TJ, Teasdale RD
 912 (2019) Retromer has a selective function in cargo sorting via endosome transport
 913 carriers. The Journal of cell biology 218:615-631.
- 914 Dotti CG, Sullivan CA, Banker GA (1988) The establishment of polarity by hippocampal
 915 neurons in culture. The Journal of neuroscience : the official journal of the Society for
 916 Neuroscience 8:1454-1468.
- 917 Fraldi A, Klein AD, Medina DL, Settembre C (2016) Brain Disorders Due to Lysosomal
 918 Dysfunction. Annual review of neuroscience 39:277-295.
- 919 Futerman AH, van Meer G (2004) The cell biology of lysosomal storage disorders.
 920 Nature reviews Molecular cell biology 5:554-565.
- 921 Garbern JY, Neumann M, Trojanowski JQ, Lee VM, Feldman G, Norris JW, Friez MJ,
 922 Schwartz CE, Stevenson R, Sima AA (2010) A mutation affecting the sodium/proton
 923 exchanger, SLC9A6, causes mental retardation with tau deposition. Brain : a journal of
 924 neurology 133:1391-1402.

- 925 Gauthier SA, Perez-Gonzalez R, Sharma A, Huang FK, Alldred MJ, Pawlik M, Kaur G,
 926 Ginsberg SD, Neubert TA, Levy E (2017) Enhanced exosome secretion in Down
 927 syndrome brain - a protective mechanism to alleviate neuronal endosomal abnormalities.
 928 *Acta neuropathologica communications* 5:65.
- 929 Ghosh P, Dahms NM, Kornfeld S (2003) Mannose 6-phosphate receptors: new twists in
 930 the tale. *Nature reviews Molecular cell biology* 4:202-212.
- 931 Gilfillan GD et al. (2008) SLC9A6 mutations cause X-linked mental retardation,
 932 microcephaly, epilepsy, and ataxia, a phenotype mimicking Angelman syndrome.
 933 *American journal of human genetics* 82:1003-1010.
- 934 Gopalakrishnan MM, Grosch HW, Locatelli-Hoops S, Werth N, Smolenova E,
 935 Nettersheim M, Sandhoff K, Hasilik A (2004) Purified recombinant human prosaposin
 936 forms oligomers that bind procathepsin D and affect its autoactivation. *The Biochemical*
 937 *journal* 383:507-515.
- 938 Gowrishankar S, Yuan P, Wu Y, Schrag M, Paradise S, Grutzendler J, De Camilli P,
 939 Ferguson SM (2015) Massive accumulation of luminal protease-deficient axonal
 940 lysosomes at Alzheimer's disease amyloid plaques. *Proceedings of the National*
 941 *Academy of Sciences of the United States of America* 112:E3699-3708.
- 942 Hasilik A, Neufeld EF (1980) Biosynthesis of lysosomal enzymes in fibroblasts.
 943 Phosphorylation of mannose residues. *The Journal of biological chemistry* 255:4946-
 944 4950.

- 945 Hirst J, Futter CE, Hopkins CR (1998) The kinetics of mannose 6-phosphate receptor
 946 trafficking in the endocytic pathway in HEp-2 cells: the receptor enters and rapidly leaves
 947 multivesicular endosomes without accumulating in a prelysosomal compartment.
 948 *Molecular biology of the cell* 9:809-816.
- 949 Huotari J, Helenius A (2011) Endosome maturation. *The EMBO journal* 30:3481-3500.
- 950 Johnson DE, Ostrowski P, Jaumouille V, Grinstein S (2016) The position of lysosomes
 951 within the cell determines their luminal pH. *The Journal of cell biology* 212:677-692.
- 952 Karim MA, Brett CL (2018) The Na⁽⁺⁾(K⁽⁺⁾)/H⁽⁺⁾ exchanger Nhx1 controls multivesicular
 953 body-vacuolar lysosome fusion. *Molecular biology of the cell* 29:317-325.
- 954 Kobayashi T, Stang E, Fang KS, de Moerloose P, Parton RG, Gruenberg J (1998) A lipid
 955 associated with the antiphospholipid syndrome regulates endosome structure and
 956 function. *Nature* 392:193-197.
- 957 Kucera A, Borg Distefano M, Berg-Larsen A, Skjeldal F, Repnik U, Bakke O, Progida C
 958 (2016) Spatiotemporal Resolution of Rab9 and CI-MPR Dynamics in the Endocytic
 959 Pathway. *Traffic (Copenhagen, Denmark)* 17:211-229.
- 960 Kucharava K, Brand Y, Albano G, Sekulic-Jablanovic M, Glutz A, Xian X, Herz J,
 961 Bodmer D, Fuster DG, Petkovic V (2020) Sodium-hydrogen exchanger 6 (NHE6)
 962 deficiency leads to hearing loss, via reduced endosomal signalling through the
 963 BDNF/Trk pathway. *Scientific reports* 10:3609.

- 964 Kulkarni VV, Maday S (2018) Neuronal endosomes to lysosomes: A journey to the
965 soma. *The Journal of cell biology* 217:2977-2979.
- 966 Laulagnier K, Schieber NL, Maritzen T, Haucke V, Parton RG, Gruenberg J (2011) Role
967 of AP1 and Gadkin in the traffic of secretory endo-lysosomes. *Molecular biology of the*
968 *cell* 22:2068-2082.
- 969 Lee JH, McBrayer MK, Wolfe DM, Haslett LJ, Kumar A, Sato Y, Lie PP, Mohan P, Coffey
970 EE, Kompella U, Mitchell CH, Lloyd-Evans E, Nixon RA (2015) Presenilin 1 Maintains
971 Lysosomal Ca(2+) Homeostasis via TRPML1 by Regulating vATPase-Mediated
972 Lysosome Acidification. *Cell reports* 12:1430-1444.
- 973 Lee JH, Yu WH, Kumar A, Lee S, Mohan PS, Peterhoff CM, Wolfe DM, Martinez-Vicente
974 M, Massey AC, Sovak G, Uchiyama Y, Westaway D, Cuervo AM, Nixon RA (2010)
975 Lysosomal proteolysis and autophagy require presenilin 1 and are disrupted by
976 Alzheimer-related PS1 mutations. *Cell* 141:1146-1158.
- 977 Levy E (2017) Exosomes in the Diseased Brain: First Insights from In vivo Studies.
978 *Frontiers in neuroscience* 11:142.
- 979 Lie PPY, Nixon RA (2019) Lysosome trafficking and signaling in health and
980 neurodegenerative diseases. *Neurobiology of disease* 122:94-105.
- 981 Lin SX, Mallet WG, Huang AY, Maxfield FR (2004) Endocytosed cation-independent
982 mannose 6-phosphate receptor traffics via the endocytic recycling compartment en route

- 983 to the trans-Golgi network and a subpopulation of late endosomes. *Molecular biology of*
 984 *the cell* 15:721-733.
- 985 Lloyd-Evans E, Haslett LJ (2016) The lysosomal storage disease continuum with ageing-
 986 related neurodegenerative disease. *Ageing research reviews* 32:104-121.
- 987 Luzio JP, Pryor PR, Bright NA (2007) Lysosomes: fusion and function. *Nature reviews*
 988 *Molecular cell biology* 8:622-632.
- 989 Marciniszyn J, Jr., Hartsuck JA, Tang J (1976) Mode of inhibition of acid proteases by
 990 pepstatin. *The Journal of biological chemistry* 251:7088-7094.
- 991 Mazzulli JR, Zunke F, Isacson O, Studer L, Krainc D (2016) alpha-Synuclein-induced
 992 lysosomal dysfunction occurs through disruptions in protein trafficking in human midbrain
 993 synucleinopathy models. *Proceedings of the National Academy of Sciences of the*
 994 *United States of America* 113:1931-1936.
- 995 Medina DL, Fraldi A, Bouche V, Annunziata F, Mansueto G, Spampinato C, Puri C,
 996 Pignata A, Martina JA, Sardiello M, Palmieri M, Polishchuk R, Puertollano R, Ballabio A
 997 (2011) Transcriptional activation of lysosomal exocytosis promotes cellular clearance.
 998 *Developmental cell* 21:421-430.
- 999 Mellman I, Fuchs R, Helenius A (1986) Acidification of the endocytic and exocytic
 1000 pathways. *Annual review of biochemistry* 55:663-700.

- 1001 Miranda AM, Lasiecka ZM, Xu Y, Neufeld J, Shahriar S, Simoes S, Chan RB, Oliveira
 1002 TG, Small SA, Di Paolo G (2018) Neuronal lysosomal dysfunction releases exosomes
 1003 harboring APP C-terminal fragments and unique lipid signatures. *Nature*
 1004 *communications* 9:291.
- 1005 Nicoli ER et al. (2019) Lysosomal Storage and Albinism Due to Effects of a De Novo
 1006 CLCN7 Variant on Lysosomal Acidification. *American journal of human genetics*
 1007 104:1127-1138.
- 1008 Ohgaki R, Matsushita M, Kanazawa H, Ogihara S, Hoekstra D, van Ijzendoorn SC
 1009 (2010) The Na⁺/H⁺ exchanger NHE6 in the endosomal recycling system is involved in
 1010 the development of apical bile canalicular surface domains in HepG2 cells. *Molecular*
 1011 *biology of the cell* 21:1293-1304.
- 1012 Ouyang Q, Joesch-Cohen L, Mishra S, Riaz HA, Schmidt M, Morrow EM (2019)
 1013 Functional Assessment In Vivo of the Mouse Homolog of the Human Ala-9-Ser NHE6
 1014 Variant. *eNeuro* 6.
- 1015 Ouyang Q, Lizarraga SB, Schmidt M, Yang U, Gong J, Ellisor D, Kauer JA, Morrow EM
 1016 (2013) Christianson syndrome protein NHE6 modulates TrkB endosomal signaling
 1017 required for neuronal circuit development. *Neuron* 80:97-112.
- 1018 Parolini I, Federici C, Raggi C, Lugini L, Palleschi S, De Mito A, Coscia C, Iessi E,
 1019 Logozzi M, Molinari A, Colone M, Tatti M, Sargiacomo M, Fais S (2009)
 1020 Microenvironmental pH is a key factor for exosome traffic in tumor cells. *The Journal of*
 1021 *biological chemistry* 284:34211-34222.

- 1022 Pescosolido MF, Stein DM, Schmidt M, El Achkar CM, Sabbagh M, Rogg JM, Tantravahi
 1023 U, McLean RL, Liu JS, Poduri A, Morrow EM (2014) Genetic and phenotypic diversity of
 1024 NHE6 mutations in Christianson syndrome. *Annals of neurology* 76:581-593.
- 1025 Peters C, Braun M, Weber B, Wendland M, Schmidt B, Pohlmann R, Waheed A, von
 1026 Figura K (1990) Targeting of a lysosomal membrane protein: a tyrosine-containing
 1027 endocytosis signal in the cytoplasmic tail of lysosomal acid phosphatase is necessary
 1028 and sufficient for targeting to lysosomes. *The EMBO journal* 9:3497-3506.
- 1029 Platt FM, Boland B, van der Spoel AC (2012) The cell biology of disease: lysosomal
 1030 storage disorders: the cellular impact of lysosomal dysfunction. *The Journal of cell*
 1031 *biology* 199:723-734.
- 1032 Platt FM, d'Azzo A, Davidson BL, Neufeld EF, Tiffet CJ (2018) Lysosomal storage
 1033 diseases. *Nature reviews Disease primers* 4:27.
- 1034 Rodriguez A, Webster P, Ortego J, Andrews NW (1997) Lysosomes behave as Ca^{2+} -
 1035 regulated exocytic vesicles in fibroblasts and epithelial cells. *The Journal of cell biology*
 1036 137:93-104.
- 1037 Scott CC, Vacca F, Gruenberg J (2014) Endosome maturation, transport and functions.
 1038 *Seminars in cell & developmental biology* 31:2-10.
- 1039 Seaman MN (2004) Cargo-selective endosomal sorting for retrieval to the Golgi requires
 1040 retromer. *The Journal of cell biology* 165:111-122.

- 1041 Sharma J, di Ronza A, Lotfi P, Sardiello M (2018) Lysosomes and Brain Health. Annual
1042 review of neuroscience 41:255-276.
- 1043 Siintola E, Partanen S, Stromme P, Haapanen A, Haltia M, Maehlen J, Lehesjoki AE,
1044 Tyynela J (2006) Cathepsin D deficiency underlies congenital human neuronal ceroid-
1045 lipofuscinosis. Brain : a journal of neurology 129:1438-1445.
- 1046 Sikora J, Leddy J, Gulinello M, Walkley SU (2016) X-linked Christianson syndrome:
1047 heterozygous female Slc9a6 knockout mice develop mosaic neuropathological changes
1048 and related behavioral abnormalities. Disease models & mechanisms 9:13-23.
- 1049 Steinfeld R, Reinhardt K, Schreiber K, Hillebrand M, Kraetzner R, Bruck W, Saftig P,
1050 Gartner J (2006) Cathepsin D deficiency is associated with a human neurodegenerative
1051 disorder. American journal of human genetics 78:988-998.
- 1052 Strauss K, Goebel C, Runz H, Mobius W, Weiss S, Feussner I, Simons M, Schneider A
1053 (2010) Exosome secretion ameliorates lysosomal storage of cholesterol in Niemann-Pick
1054 type C disease. The Journal of biological chemistry 285:26279-26288.
- 1055 Stromme P, Dobrenis K, Sillitoe RV, Gulinello M, Ali NF, Davidson C, Micsenyi MC,
1056 Stephney G, Ellevog L, Klungland A, Walkley SU (2011) X-linked Angelman-like
1057 syndrome caused by Slc9a6 knockout in mice exhibits evidence of endosomal-
1058 lysosomal dysfunction. Brain : a journal of neurology 134:3369-3383.
- 1059 van Weert AW, Dunn KW, Geuze HJ, Maxfield FR, Stoorvogel W (1995) Transport from
1060 late endosomes to lysosomes, but not sorting of integral membrane proteins in

1061 endosomes, depends on the vacuolar proton pump. The Journal of cell biology 130:821-
1062 834.

1063 Vazquez CL, Colombo MI (2009) Assays to assess autophagy induction and fusion of
1064 autophagic vacuoles with a degradative compartment, using monodansylcadaverine
1065 (MDC) and DQ-BSA. Methods in enzymology 452:85-95.

1066 Verweij FJ et al. (2018) Quantifying exosome secretion from single cells reveals a
1067 modulatory role for GPCR signaling. The Journal of cell biology 217:1129-1142.

1068 Vidoni C, Follo C, Savino M, Melone MA, Isidoro C (2016) The Role of Cathepsin D in
1069 the Pathogenesis of Human Neurodegenerative Disorders. Medicinal research reviews
1070 36:845-870.

1071 Villarroya-Beltri C, Baixauli F, Mittelbrunn M, Fernandez-Delgado I, Torralba D, Moreno-
1072 Gonzalo O, Baldanta S, Enrich C, Guerra S, Sanchez-Madrid F (2016) ISGylation
1073 controls exosome secretion by promoting lysosomal degradation of MVB proteins.
1074 Nature communications 7:13588.

1075 von Figura K, Hasilik A (1986) Lysosomal enzymes and their receptors. Annual review of
1076 biochemistry 55:167-193.

1077 Winckler B, Faundez V, Maday S, Cai Q, Guimas Almeida C, Zhang H (2018) The
1078 Endolysosomal System and Proteostasis: From Development to Degeneration. The
1079 Journal of neuroscience : the official journal of the Society for Neuroscience 38:9364-
1080 9374.

1081 Yap CC, Digilio L, McMahon LP, Garcia ADR, Winckler B (2018) Degradation of
1082 dendritic cargos requires Rab7-dependent transport to somatic lysosomes. The Journal
1083 of cell biology 217:3141-3159.

1084 Zaidi N, Maurer A, Nieke S, Kalbacher H (2008) Cathepsin D: a cellular roadmap.
1085 Biochemical and biophysical research communications 376:5-9.

1086

1087 **FIGURE LEGEND**

1088 **Figure 1.** Decreased lysosomal proteolysis in *Nhe6*-null neurons *in vitro*. (A) Puncta
 1089 analysis by fluorescence microscopy and 3D images of WT and *Nhe6*^{-/-} male primary
 1090 hippocampal neurons following DQ-BSA treatment at DIV 5. Images are denoted as: 2D
 1091 (i.e. DQ-BSA fluorescent microscopy maximum intensity projection images), 3D (i.e. 3D
 1092 reconstruction of DQ-BSA puncta), and 3D Rotation (i.e. 3D image rotated 90° along the
 1093 x axis). (B-E) Quantification of 3D-reconstructed DQ-BSA puncta. (B) Number of DQ-
 1094 BSA puncta per cell (WT n=50 cells from 5 mice, *Nhe6*^{-/-} n=50 cells from 5 mice, 4
 1095 litters, p=0.02, Glass's delta=0.46). (C) Average DQ-BSA puncta volume per cell (WT
 1096 n=50 cells from 5 mice, *Nhe6*^{-/-} n=49 cells from 5 mice, 4 litters, p=0.002, Cohen's
 1097 d=0.54). (D) Total summed DQ-BSA puncta volume per cell (WT n=50 cells from 5 mice,
 1098 *Nhe6*^{-/-} n=49 cells from 5 mice, 4 litters, p=0.01, Glass's delta=0.58). (E) Average
 1099 distance of DQ-BSA puncta from nucleus (WT n=50 cells from 5 mice, *Nhe6*^{-/-} n=49 cells
 1100 from 5 mice, 4 litters). (F) Confocal microscopy images of male WT and *Nhe6*-null
 1101 littermate primary hippocampal neurons following DQ-BSA treatment at DIV 3, 5, and 14.
 1102 (G) Quantification of mean fluorescence intensity (MFI) at 3 DIV (WT n=160 cells, *Nhe6*^{-/-}
 1103 n=156 cells, 5 mice per genotype, 4 litters, p=0.04, Cohen's d=0.23), 5 DIV (WT n=138
 1104 cells, *Nhe6*^{-/-} n=143 cells, 5 mice per genotype, 4 litters, p<0.0001, Glass's delta=0.58),
 1105 14 DIV (WT n=78 cells, *Nhe6*^{-/-} n=80 cells, 4 mice per genotype, 4 litters, p<0.0001,
 1106 Cohen's d=0.64). Some primary neurons at 5 DIV were analyzed in both 3D-
 1107 reconstruction and MFI data. (H) Fluorescence microscopy images of WT and *Nhe6*^{-/-}
 1108 male primary hippocampal neurons following BSA-AF594 treatment at 14 DIV. (I)
 1109 Quantification of MFI at 3 DIV (WT n=42 cells, *Nhe6*^{-/-} n=43 cells, 5 mice per genotype,
 1110 5 litters), 5 DIV (WT n=40 cells, *Nhe6*^{-/-} n=40 cells, 5 mice per genotype, 5 litters), 14
 1111 DIV (WT n=40 cells, *Nhe6*^{-/-} n=40 cells, 5 mice per genotype, 5 litters). Nuclei are
 1112 marked in blue by Hoechst. Scale bars = 5 μm (A and H) or 10 μm (F). Data reported as

mean \pm SEM. Unpaired two-tailed Student's t-test (G: 3 and 14 DIV, I: 3 DIV) or Mann-Whitney test (B-E, G: 5 DIV, I: 5 and 14 DIV).

1115

1116 **Figure 2.** Loss of NHE6 impairs lysosome enzyme function *in vitro* and *ex vivo*. (A)

1117 Confocal microscopy images of mature cathepsin D using BODIPY Pepstatin-A in WT

1118 and Nhe6^{-/-} male mouse primary hippocampal neurons at DIV 3, 5, and 14. (B)

1119 Quantification of mean fluorescence intensity (MFI) per cell at 3 DIV (WT n=153 cells,

1120 Nhe6^{-/-} n=148 cells, 5 mice per genotype, 5 litters), 5 DIV (WT n=130 cells, Nhe6^{-/-}

1121 n=129 cells, 5 mice per genotype, 3 litters, p<0.0001, Cohen's d=0.66), and 14 DIV (WT

1122 n=80 cells, Nhe6^{-/-} n=80 cells, 4 mice per genotype, 4 litters, p<0.0001, Cohen's

1123 d=0.76). (C) Quantification of number (#) of puncta per cell at 3 DIV (WT n=161 cells,

1124 Nhe6^{-/-} n=148 cells, 5 mice per genotype, 5 litters), 5 DIV (WT n=107 cells, Nhe6^{-/-}

1125 n=105 cells, 4 mice per genotype, 3 litters, p=0.001, Glass's delta=0.37), 14 DIV (WT

1126 n=78 cells, Nhe6^{-/-} n=78 cells from, 4 mice per genotype, 4 litters, p<0.0001, Cohen's

1127 d=0.56). (D and E) Cathepsin D western blot (D) and quantification (E) in WT and Nhe6^{-/-}

1128 ^{-/-} male littermate mice, acutely dissected hippocampal tissue at 8 weeks old (WT n=11

1129 animals, Nhe6^{-/-} n=6 animals, 6 litters, cleaved CatD p=0.003, Hedges's g=1.77). (F) β -

1130 N-Acetylglucosaminidase and (G) acid phosphatase enzyme activity in Nhe6^{-/-} male

1131 littermate mice, acutely dissected brain tissue (cerebellum, CB; cortex, CT;

1132 hippocampus, HP; HP p=0.047, Hedges's g=0.78) at 8 weeks old as well as primary

1133 hippocampal neurons at 14 DIV relative to male WT littermates (hippocampal culture,

1134 HP-C, p=0.044, Hedges's g=1.42). The sample sizes are as follows: B-NAG brain tissue

1135 (WT n=9 animals, Nhe6^{-/-} n=6 animals, 6 litters), B-NAG hippocampal culture (WT n=6

1136 animals, Nhe6^{-/-} n=6 animals, 6 litters), acid phosphatase brain tissue (WT n=7 animals,

1137 Nhe6^{-/-} n=5 animals, 5 litters), and acid phosphatase hippocampal culture (WT n=5

1138 animals, Nhe6^{-/-} n=5 animals, 5 litters). Values are expressed as the percentage of

1139 Nhe6^{-/-} activity relative to its WT male littermate activity. Nuclei are marked in blue by
 1140 Hoechst. Scale bars = 5 μ m. Data reported as mean \pm SEM. A.U.=Arbitrary units.
 1141 CB=Cerebellum, CT=Cortex, HP=Hippocampus, HP-C=Hippocampal cultures. One-
 1142 sample Student's t-test with a hypothetical mean=1 (F, G), unpaired two-tailed Student's
 1143 t-test (E), or Mann-Whitney test (B, C).
 1144
 1145 **Figure 3.** Intra-luminal lysosome pH more acidic in NHE6-null neurons. (A) Single-plane
 1146 confocal microscopy images of lysosome pH loaded with fluorescent dextrans (i.e. pH-
 1147 sensitive Oregon green 488-dextran and pH-insensitive tetramethylrhodamine-dextran)
 1148 in male WT and Nhe6-null mouse primary hippocampal neurons at DIV 8. (B)
 1149 Quantification of intra-luminal lysosome pH in soma and processes (WT n=11 animals,
 1150 Nhe6^{-/-} n=10 animals, 5 litters, Soma: p=0.002, Hedges's g =1.43, Processes: p=0.002,
 1151 Hedges's g =1.60). (C) Single-plane confocal microscopy images of lysosome pH loaded
 1152 with fluorescent dextrans (i.e. pH-sensitive Oregon green 488-dextran and pH-
 1153 insensitive tetramethylrhodamine-dextran) following bafilomycin A1 treatment (100 nm)
 1154 in male WT and Nhe6-null mouse primary hippocampal neurons at DIV 8. (D)
 1155 Quantification of intra-luminal lysosome pH in soma and processes following bafilomycin
 1156 A1 treatment (WT n=4 animals, Nhe6^{-/-} n=7 animals, 3 litters). (E) Single-plane confocal
 1157 microscopy images of endosome pH loaded with fluorescent transferrin (i.e. pH-sensitive
 1158 FITC-transferrin and pH-insensitive Alexa Fluor 546-transferrin) in male WT and Nhe6-
 1159 null mouse primary hippocampal neurons at DIV 5. (F) Quantification of luminal
 1160 endosome pH in soma and processes (WT n=21, Nhe6^{-/-} n=22, 13 litters, Soma: p=0.04,
 1161 Cohen's d =0.66, Processes: p=0.01, Cohen's d =0.83). Orange arrows denote soma
 1162 while yellow arrowheads denote processes. Scale bars = 50 μ m. Data reported as

mean \pm SEM. Unpaired two-tailed Student's t-test (B: processes, F) with Welch's correction (D: soma) or Mann-Whitney test (B: soma).

Figure 4. Loss of NHE6 alters cathepsin D activation and distribution across the endosome and lysosome compartment. Confocal microscopy single-plane images of BODIPY Pepstatin-A colocalization with different endosomes and the lysosome in male WT and Nhe6-null mouse primary hippocampal neurons at DIV 5 and 14. Colocalization of active CatD within distinct endosome and lysosome compartments was tested using BODIPY pepstatin-A colocalization with the following markers: (A) dextran (lysosome), (C) LAMP1 (lysosome and late endosome), (E) RAB7 (late endosome), (G) LBPA (late endosome), and (I) RAB5 (early endosome). BODIPY pepstatin-A colocalization with these markers was quantified using the Manders' coefficient (i.e. degree BODIPY pepstatin-A signal overlaps with marker signal or M1). (B) Quantification of BODIPY pepstatin-A colocalization with dextran at 5 DIV (WT n=50 cells, Nhe6^{-/-} n=50 cells, 5 mice per genotype, 3 litters, p=0.004, Cohen's *d*=0.58) and 14 DIV (WT n=40 cells from 4 mice, Nhe6^{-/-} n=50 cells from 5 mice, 3 litters, p=0.0004, Cohen's *d*=0.78). (D) Quantification of BODIPY pepstatin-A colocalization with LAMP1 at 5 DIV (WT n=50 cells, Nhe6^{-/-} n=50 cells, 5 mice per genotype, 4 litters, p=0.018, Cohen's *d*=0.48) and 14 DIV (WT n=40 cells, Nhe6^{-/-} n=40 cells, 4 mice per genotype, 3 litters, p<0.0001, Cohen's *d*=1.06). (F) Quantification of BODIPY pepstatin-A colocalization with RAB7 at 5 DIV (WT n=60 cells, Nhe6^{-/-} n=60 cells, 6 mice per genotype, 4 litters, p=0.0004, Cohen's *d*=0.66) and 14 DIV (WT n=50 cells, Nhe6^{-/-} n=50 cells, 5 mice per genotype, 3 litters, p<0.0001, Cohen's *d*=0.95). (H) Quantification of BODIPY pepstatin-A colocalization with LBPA at 5 DIV (WT n=40 cells, Nhe6^{-/-} n=40 cells, 4 mice per genotype, 3 litters, p<0.0003, Cohen's *d*=0.82) and 14 DIV (WT n=70 cells, Nhe6^{-/-} n=70 cells, 6 mice per genotype, 4 litters). (J) Quantification of BODIPY pepstatin-A

1189 colocalization with RAB5 at 5 DIV (WT n=50 cells from 5 mice, Nhe6^{-/-} n=60 cells from 6
 1190 mice, 4 litters, p=0.009, Cohen's $d=0.49$) and 14 DIV (WT n=40 cells from 4 mice, Nhe6^{-/-}
 1191 ^{-/-} n=50 cells from 5 mice, 3 litters). (K and L) Cathepsin D western blot (K) and
 1192 quantification (L) in lysosome-enriched fractions (LEF) from acutely dissected 4-month-
 1193 old WT and Nhe6^{-/-} male littermate hippocampus and neocortex combined (WT n=10,
 1194 Nhe6^{-/-} n=8, 7 litters, pro CatD p=0.007, Hedges's $g=1.26$, cleaved CatD p=0.0007,
 1195 Hedges's $g=1.99$). Cathepsin D was normalized to LAMP1. Scale bars = 10 μ m. BOD =
 1196 BODIPY-Pepstatin A, DEX = Dextran, LAMP1 = LAMP1. Data reported as mean \pm SEM.
 1197 Unpaired two-tailed Student's t-test (B, D, F: 14 DIV, L: cleaved CatD) or Mann-Whitney
 1198 test (F: 5 DIV, H, J, L: pro-CatD).

1199

1200 **Figure 5.** Larger lysosome-associated dextran puncta in mature NHE6-null neurons. (A)
 1201 Confocal microscopy images of WT and Nhe6^{-/-} male primary hippocampal neurons
 1202 following dextran treatment at DIV 5. Images are denoted as 2D (i.e. fluorescent
 1203 microscopy images) and 3D (i.e. 3D reconstruction of dextran puncta). (B) Quantification
 1204 of 3D-reconstructed dextran puncta at DIV 5 (WT n=50 cells from 5 mice, Nhe6^{-/-} n=40
 1205 cells from 4 mice, 3 litters). Graphs depict the following: number of dextran puncta per
 1206 cell, average dextran puncta volume per cell, and total summed dextran puncta volume
 1207 per cell. (C) Confocal microscopy images of WT and Nhe6^{-/-} male primary hippocampal
 1208 neurons following dextran treatment at DIV 14. (D) Quantification of 3D-reconstructed
 1209 dextran puncta at DIV 14 (WT n=40 cells from 4 mice, Nhe6^{-/-} n=50 cells from 5 mice, 3
 1210 litters). Graphs depict the following: number of dextran puncta per cell, average dextran
 1211 puncta volume per cell (p=0.04, Glass's $\Delta=0.87$), and total summed dextran puncta
 1212 volume per cell (Welch's correction). Scale bars = 5 μ m. Data reported as mean \pm SEM.

1213 Unpaired two-tailed Student's t-test (D: number of M6PR puncta and average M6PR
 1214 puncta volume-transformed) or Mann-Whitney test (B, D: total M6PR puncta volume).
 1215

1216 **Figure 6.** LAMP1 dysfunction in NHE6-null neurons. (A) LAMP1 western blot and
 1217 quantification in WT and Nhe6^{-/-} male littermate mice, acutely dissected hippocampal
 1218 tissue at 8 weeks old (WT n=9 animals, Nhe6^{-/-} n=5 animals, 5 litters). (B) LAMP1
 1219 western blot and quantification in WT and Nhe6^{-/-} male primary hippocampal neurons at
 1220 14 DIV (WT n=5 animals, Nhe6^{-/-} n=5 animals, 5 litters). (C) Confocal microscopy
 1221 images of WT and Nhe6^{-/-} male primary hippocampal neurons at 5 DIV labelled with
 1222 LAMP1 antibody. Images are denoted as 2D (i.e. fluorescent microscopy images) and
 1223 3D (i.e. 3D reconstruction of LAMP1 puncta). (D) Quantification of 3D-reconstructed
 1224 LAMP1 puncta at DIV 5 (WT n=50 cells, Nhe6^{-/-} n=50 cells, 5 mice per genotype, 3
 1225 litters). Graphs depict the following: number of LAMP1 puncta per cell (p=0.02, Cohen's
 1226 $d=0.42$), average LAMP1 puncta volume per cell, and total summed LAMP1 puncta
 1227 volume per cell (p=0.03, Cohen's $d=0.42$). (E) Confocal microscopy images of WT and
 1228 Nhe6^{-/-} male primary hippocampal neurons at 14 DIV labelled with LAMP1 antibody. (F)
 1229 Quantification of 3D-reconstructed LAMP1 puncta at DIV 14 (WT n=40 cells, Nhe6^{-/-}
 1230 n=40 cells, 4 mice per genotype, 3 litters). Graphs depict the following: number of
 1231 LAMP1 puncta per cell (p=0.01, Cohen's $d=0.58$), average LAMP1 puncta volume per
 1232 cell (p=0.01, Glass's $\delta=0.69$), and total summed LAMP1 puncta volume per cell.
 1233 Scale bars = 5 μ m. Data reported as mean \pm SEM. Unpaired two-tailed Student's t-test
 1234 (A, B, F: number of LAMP1 puncta and total LAMP1 puncta volume) with Welch's
 1235 correction (F: average LAMP1 puncta volume) or Mann-Whitney test (D).

1236

1237 **Figure 7.** Greater RAB7 puncta volume in NHE6-null neurons. (A) RAB7 western blot
 1238 and quantification in WT and Nhe6^{-/-} male littermate mice, acutely dissected

1239 hippocampal tissue at 8 weeks old (WT n=11 animals, Nhe6^{-/-} n=6 animals, 6 litters). (B)
 1240 RAB7 western blot and quantification in WT and Nhe6^{-/-} male primary hippocampal
 1241 neurons at 14 DIV (WT n=5 animals, Nhe6^{-/-} n=5 animals, 5 litters). (C) Confocal
 1242 microscopy images of WT and Nhe6^{-/-} male primary hippocampal neurons at 5 DIV
 1243 labelled with RAB7 antibody. Images are denoted as 2D (i.e. fluorescent microscopy
 1244 images) and 3D (i.e. 3D reconstruction of RAB7 puncta). (D) Quantification of 3D-
 1245 reconstructed RAB7 puncta at DIV 5 (WT n=50 cells, Nhe6^{-/-} n=50 cells, 5 mice per
 1246 genotype, 3 litters). Graphs depict the following: number of RAB7 puncta per cell,
 1247 average RAB7 puncta volume per cell (p=0.01, Cohen's *d*=0.51), and total summed
 1248 RAB7 puncta volume per cell (p=0.04, Cohen's *d*=0.38). (E) Confocal microscopy
 1249 images of WT and Nhe6^{-/-} male primary hippocampal neurons at 14 DIV labelled with
 1250 RAB7 antibody. (F) Quantification of 3D-reconstructed RAB7 puncta at DIV 14 (WT n=40
 1251 cells from 4 mice, Nhe6^{-/-} n=50 cells from 5 mice, 3 litters). Graphs depict the following:
 1252 number of RAB7 puncta per cell, average RAB7 puncta volume per cell, and total
 1253 summed RAB7 puncta volume per cell. Scale bars = 5 μ m. Data reported as
 1254 mean \pm SEM. Unpaired two-tailed Student's t-test (A, B, D: number of Rab7 puncta and
 1255 average RAB7 puncta volume, F: Rab7 puncta) with Welch's correction (F: total RAB7
 1256 puncta volume) or Mann-Whitney test (D: total RAB7 puncta volume, F: average RAB7
 1257 puncta volume).

1258

1259 **Figure 8.** RAB5 features unaffected by loss of NHE6. (A) RAB5 western blot and
 1260 quantification in WT and Nhe6^{-/-} male littermate mice, acutely dissected hippocampal
 1261 tissue at 8 weeks old (WT n=9 animals, Nhe6^{-/-} n=6 animals, 6 litters). (B) RAB5
 1262 western blot and quantification in WT and Nhe6^{-/-} male primary hippocampal neurons at
 1263 14 DIV (WT n=5 animals, Nhe6^{-/-} n=5 animals, 5 litters). (C) Confocal microscopy

1264 images of WT and Nhe6^{-/-} male primary hippocampal neurons at 5 DIV labelled with
 1265 RAB5 antibody. Images are denoted as 2D (i.e. fluorescent microscopy images) and 3D
 1266 (i.e. 3D reconstruction of RAB5 puncta). (D) Quantification of 3D-reconstructed RAB5
 1267 puncta at DIV 5 (WT n=50 cells, Nhe6^{-/-} n=50 cells, 5 mice per genotype, 4 litters).
 1268 Graphs depict the following: number of RAB5 puncta per cell, average RAB5 puncta
 1269 volume per cell, and total summed RAB5 puncta volume per cell. (E) Confocal
 1270 microscopy images of WT and Nhe6^{-/-} male primary hippocampal neurons at 14 DIV
 1271 labelled with RAB5 antibody. (F) Quantification of 3D-reconstructed RAB5 puncta at DIV
 1272 14 (WT n=50 cells, Nhe6^{-/-} n=50 cells, 5 mice per genotype, 3 litters). Graphs depict the
 1273 following: number of RAB5 puncta per cell, average RAB5 puncta volume per cell, and
 1274 total summed RAB5 puncta volume per cell. Scale bars = 5 μ m. Data reported as
 1275 mean \pm SEM. Unpaired two-tailed Student's t-test (A, B) with Welch's correction (F:
 1276 average RAB5 puncta volume and total RAB5 puncta volume) or Mann-Whitney test (D,
 1277 F: number of Rab5 puncta).

1278

1279 **Figure 9.** Greater M6PR puncta volume in mature NHE6-null neurons. (A) M6PR
 1280 western blot and quantification in WT and Nhe6^{-/-} male littermate mice, acutely dissected
 1281 hippocampal tissue at 8 weeks old (WT n=11 animals, Nhe6^{-/-} n=6 animals, 6 litters). (B)
 1282 M6PR western blot and quantification in WT and Nhe6^{-/-} male primary hippocampal
 1283 neurons at 14 DIV (WT n=4 animals, Nhe6^{-/-} n=4 animals, 4 litters). (C) Confocal
 1284 microscopy images of WT and Nhe6^{-/-} male primary hippocampal neurons at 5 DIV
 1285 labelled with M6PR antibody. Images are denoted as 2D (i.e. fluorescent microscopy
 1286 images) and 3D (i.e. 3D reconstruction of M6PR puncta). (D) Quantification of 3D-
 1287 reconstructed M6PR puncta at DIV 5 (WT n=50 cells, Nhe6^{-/-} n=50 cells, 5 mice per
 1288 genotype, 3 litters). Graphs depict the following: number of M6PR puncta per cell,

average M6PR puncta volume per cell, and total summed M6PR puncta volume per cell.

(E) Confocal microscopy images of WT and *Nhe6^{-/-}* male primary hippocampal neurons at 14 DIV labelled with M6PR antibody. (F) Quantification of 3D-reconstructed M6PR puncta at DIV 14 (WT n=70 cells from 7 mice, *Nhe6^{-/-}* n=80 cells from 8 mice, 6 litters). Graphs depict the following: number of M6PR puncta per cell ($p=0.05$, Glass's $\Delta=0.44$), average M6PR puncta volume per cell, and total summed M6PR puncta volume per cell ($p=0.004$, Cohen's $d=0.41$). Scale bars = 5 μm . Data reported as mean \pm SEM. Unpaired two-tailed Student's t-test (A, B, D: number of M6PR puncta and total M6PR puncta volume) or Mann-Whitney test (D: average M6PR puncta volume, F).

Figure 10. Altered mannose 6-phosphate receptor (M6PR) distribution in NHE6-null neurons *in vitro*. Confocal microscopy single-plane images of M6PR colocalization with different markers of the endosome and lysosome compartment in male WT and *Nhe6*-null mouse primary hippocampal neurons at DIV 5 and 14. Colocalization of M6PR was tested using the following markers: (A) TGN46 (*trans*-Golgi network), (C) RAB7 (late endosome), and (E) LAMP1 (late endosome), and (G) RAB5 (early endosome). M6PR colocalization with these markers was quantified using the Manders' coefficient (i.e. degree M6PR signal overlaps with marker signal or M1). (B) Quantification of M6PR colocalization with TGN46 at 5 DIV (WT n=70 cells, *Nhe6^{-/-}* n=70 cells, 7 mice per genotype, 4 litters, $p=0.01$, Cohen's $d=0.43$) and 14 DIV (WT n=60 cells from 6 mice, *Nhe6^{-/-}* n=60 cells from 6 mice, 4 litters, $p=0.009$, Cohen's $d=0.50$). (D) Quantification of M6PR with RAB7 at 5 DIV (WT n=50 cells, *Nhe6^{-/-}* n=50 cells, 5 mice per genotype, 3 litters, $p=0.0008$, Cohen's $d=0.71$) and 14 DIV (WT n=40 cells, *Nhe6^{-/-}* n=40 cells, 4 mice per genotype, 3 litters, $p=0.003$, Cohen's $d=0.72$). (F) Quantification of M6PR with LAMP1 at 5 DIV (WT n=60 cells from 6 mice, *Nhe6^{-/-}* n=70 cells from 7 mice, 4 litters,

1314 $p=0.03$, Cohen's $d=0.40$) and 14 DIV (WT $n=40$ cells from 4 mice, $Nhe6^{-/-}$ $n=50$ cells
 1315 from 5 mice, 3 litters, $p<0.0001$, Cohen's $d=1.03$). (H) Quantification of M6PR
 1316 colocalization with RAB5 at 5 DIV (WT $n=50$ cells from 5 mice, $Nhe6^{-/-}$ $n=60$ cells from 6
 1317 mice, 4 litters, $p=0.009$, Glass's $\delta=0.64$) and 14 DIV (WT $n=40$ cells, $Nhe6^{-/-}$ $n=40$
 1318 cells, 4 mice per genotype, 2 litters). Scale bars = 10 μm . Data reported as mean \pm SEM.
 1319 Unpaired two-tailed Student's t-test (F: 14 DIV) or Mann-Whitney test (B, D, F: 5 DIV, H).

1320

1321 **Figure 11.** Delayed endosome-lysosome fusion in NHE6-null neurons *in vitro*. (A) Live-
 1322 cell confocal microscopy imaging of endosome-lysosome fusion in WT and $Nhe6^{-/-}$ male
 1323 mouse primary hippocampal neurons at 5 DIV with and without bafilomycin A treatment.
 1324 The following time points were measured following incubation with Alexa Fluor 647-
 1325 dextran: 0, 20, 40, 60, 80, 100, and 120 minutes. (B) Quantification of endosome-
 1326 lysosome fusion (WT $n=7$ animals, $Nhe6^{-/-}$ $n=7$ animals, 5 litters). Endosome-lysosome
 1327 fusion % are expressed as % fold change to time point 0 for the same animal. There was
 1328 a significant interaction effect for time x genotype (F [6, 72.0], = 3.432, $p = 0.005$). Scale
 1329 bars = 5 μm . Data reported as mean \pm SEM. Linear mixed model.

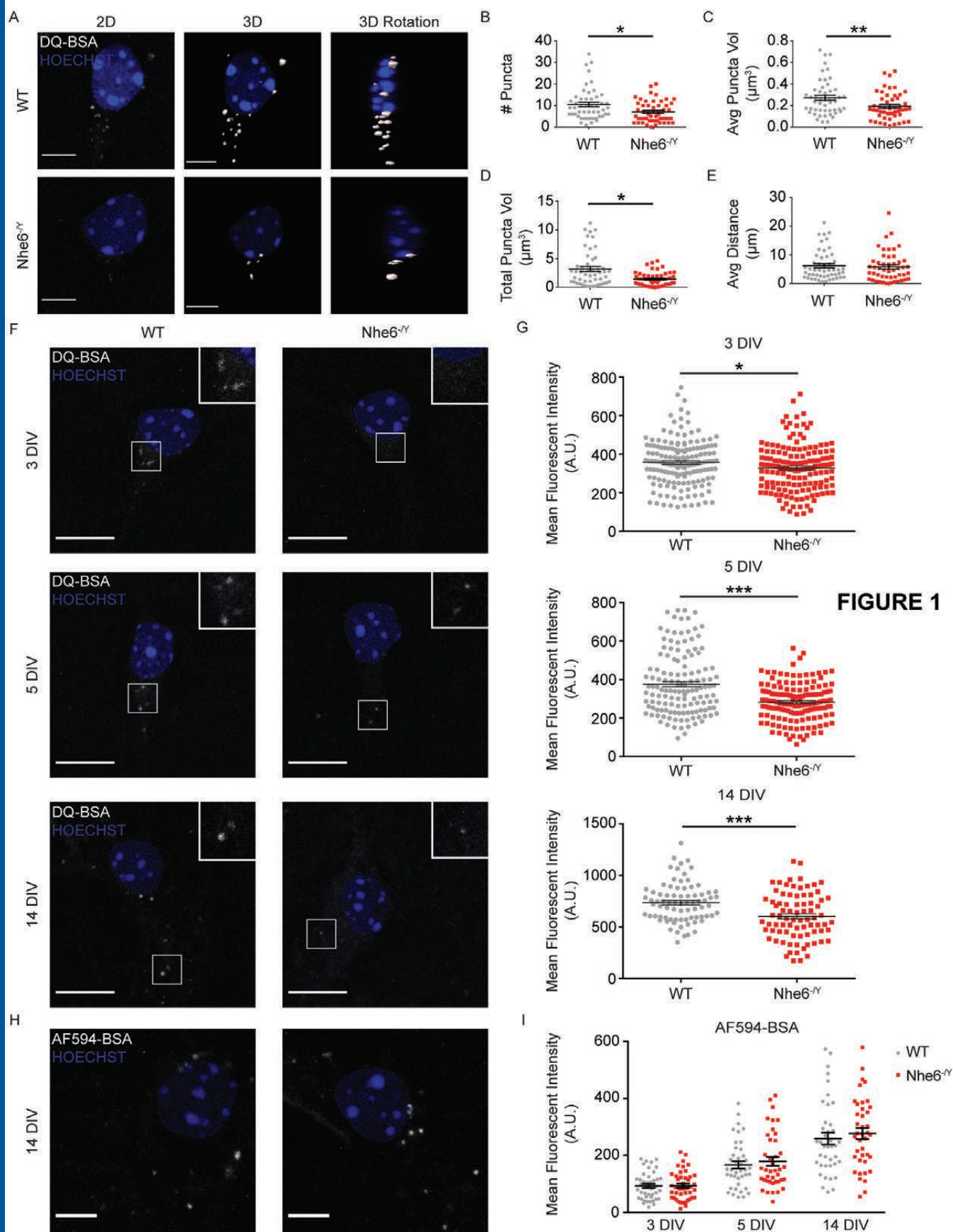
1330

1331 **Figure 12.** Loss of NHE6 increases multivesicular body fusion (MVB) with the plasma
 1332 membrane (PM) and exosome secretion. (A) Representative TIRF image depicting
 1333 MVB-PM fusion and exosome release as developed from Verweij et al. (2018). Widefield
 1334 image of neuron co-transfected with mCherry and CD63-pHluorin expression constructs.
 1335 White inset shows location of MVB-PM fusion and the zoomed in panels on the right.
 1336 Each panel represents the progression of a CD63-pHluorin fusion event with the plasma
 1337 membrane with the number of seconds indicated below the panel. Large scale bar = 10
 1338 μm , small scale bar = 1 μm . (B) Quantification of full MVB-PM fusion/exosome release

1339 events per cell over 5 minutes in WT and Nhe6^{-/-} male littermate mouse primary
 1340 hippocampal neurons at 14 DIV (WT n=28 cells from 7 mice, Nhe6^{-/-} n=18 cells from 7
 1341 mice, 5 litters, p=0.009, Glass's delta=2.27). (C) Quantification of full MVB-PM
 1342 fusion/exosome release events per cell over 5 minutes in WT and Nhe6^{-/-} male mouse
 1343 primary hippocampal neurons at 14 DIV under the following conditions: untreated (same
 1344 as B), U18666A (positive control) (WT n=14 cells from 5 mice, Nhe6^{-/-} n=14 cells from 5
 1345 mice, 3 litters), bafilomycin A1 (positive control) (WT n=14 cells from 7 mice, Nhe6^{-/-}
 1346 n=16 cells from 6 mice, 4 litters, Kruskal-Wallis test with Dunn's test: WT untreated
 1347 compared to WT bafilomycin A1 p=0.002, Glass's delta=3.04). (D and E) CD63 western
 1348 blot (D) and quantification (E) in WT and Nhe6^{-/-} male littermate mouse primary
 1349 hippocampal neurons at 14 DIV (WT n=5 cultures, Nhe6^{-/-} n=5 cultures, 5 litters, p=0.02,
 1350 Glass's delta=1.68). (F) Released b-hexosaminidase enzyme activity following short-
 1351 term incubation in Tyrode's solution followed by treatment with either ionomycin or
 1352 DMSO (WT n=9, Nhe6^{-/-} n=9, 8 litters). (G) Released cathepsin D enzyme activity
 1353 following short-term incubation in Tyrode's solution followed by treatment with either
 1354 ionomycin or DMSO (WT n=6, Nhe6^{-/-} n=6, 5 litters). (H) Released LDH activity across
 1355 all b-hexosaminidase (WT n=5, Nhe6^{-/-} n=5, 5 litters) and cathepsin D (WT n=4, Nhe6^{-/-}
 1356 n=4, 3 litters) experiments. Data reported as mean±SEM. Unpaired two-tailed Student's
 1357 t-test (C: WT-Nhe6^{-/-}: bafilomycin A1) with Welch's correction (E), Mann-Whitney test (B,
 1358 C: WT-Nhe6^{-/-}: U18666A), Kruskal-Wallis test with Dunn's test (C: differences between
 1359 treatments by genotype), two-way ANOVA with Tukey's multiple comparisons test (F, G,
 1360 H).

1361
 1362 **Figure 13.** NHE6-null endolysosomal model in neurons. (A) Schematic representation of
 1363 endosomal maturation and trafficking in WT neurons. Newly synthesized CatD enzymes

1364 are trafficked through the endocytic pathway by M6PRs until they reach the highly acidic
1365 lysosome lumen to assist in degradation, ensuring proper lysosome functioning. (B) Loss
1366 of NHE6 leads to overacidification of both the endosomal and lysosomal lumen that
1367 ultimately results in lysosome dysfunction. CatD becomes prematurely active in hyper-
1368 acidified endosomal compartments yet is less likely to be trafficked and active in
1369 lysosomes, likely due in part to impaired endosome-lysosome fusion. Trafficking of
1370 M6PRs, which are responsible for delivering newly synthesized CatD to lysosomes, is
1371 also disrupted as they accumulate in endosomes and are unable to be transported back
1372 to the TGN. Endolysosomal trafficking is further altered as multivesicular bodies are
1373 more likely to fuse with the plasma membrane, resulting in enhanced exosome release.
1374
1375 **Movie 1.** Multivesicular body (MVB) fusion with the plasma membrane (PM) and
1376 exosome release.



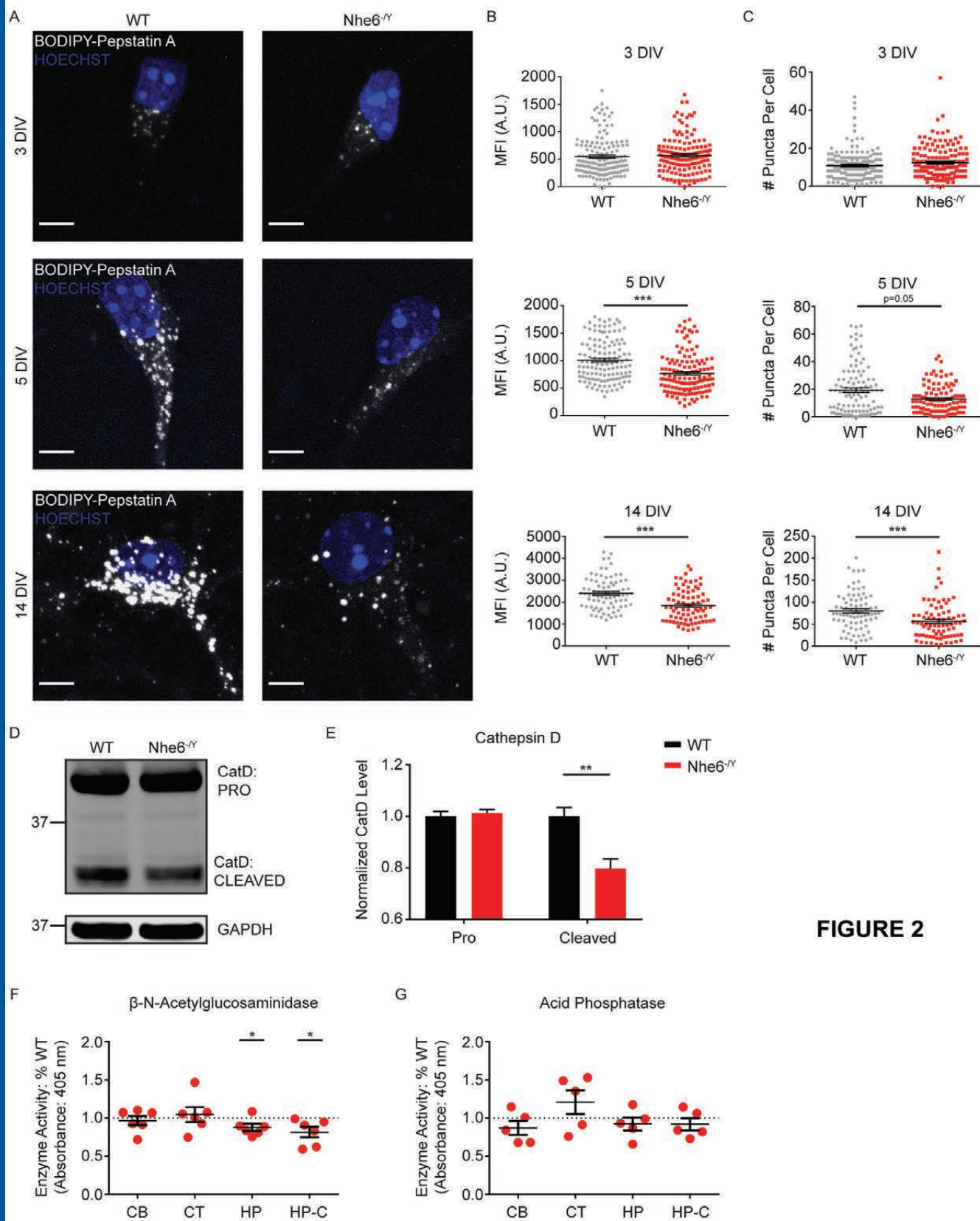


FIGURE 2

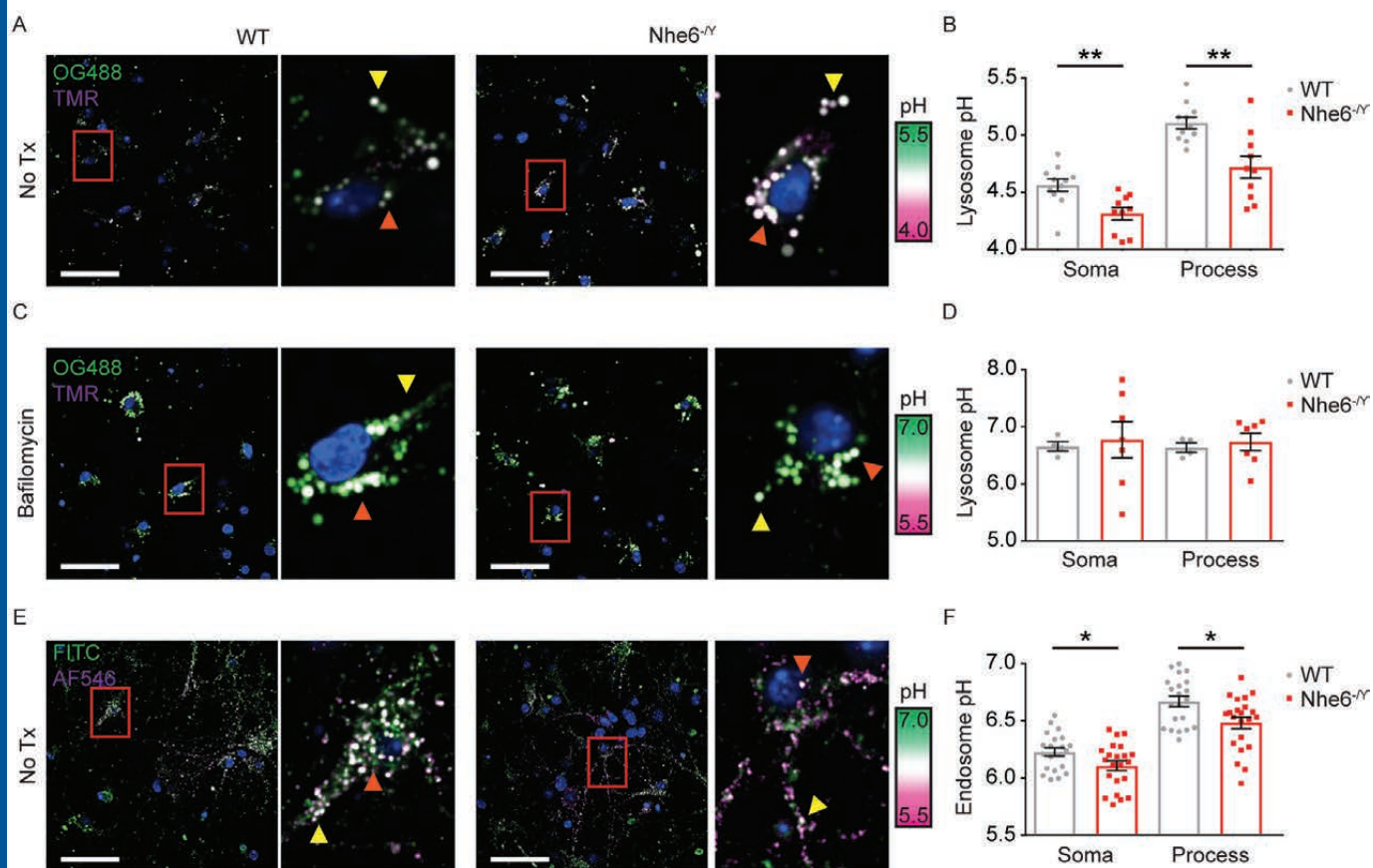
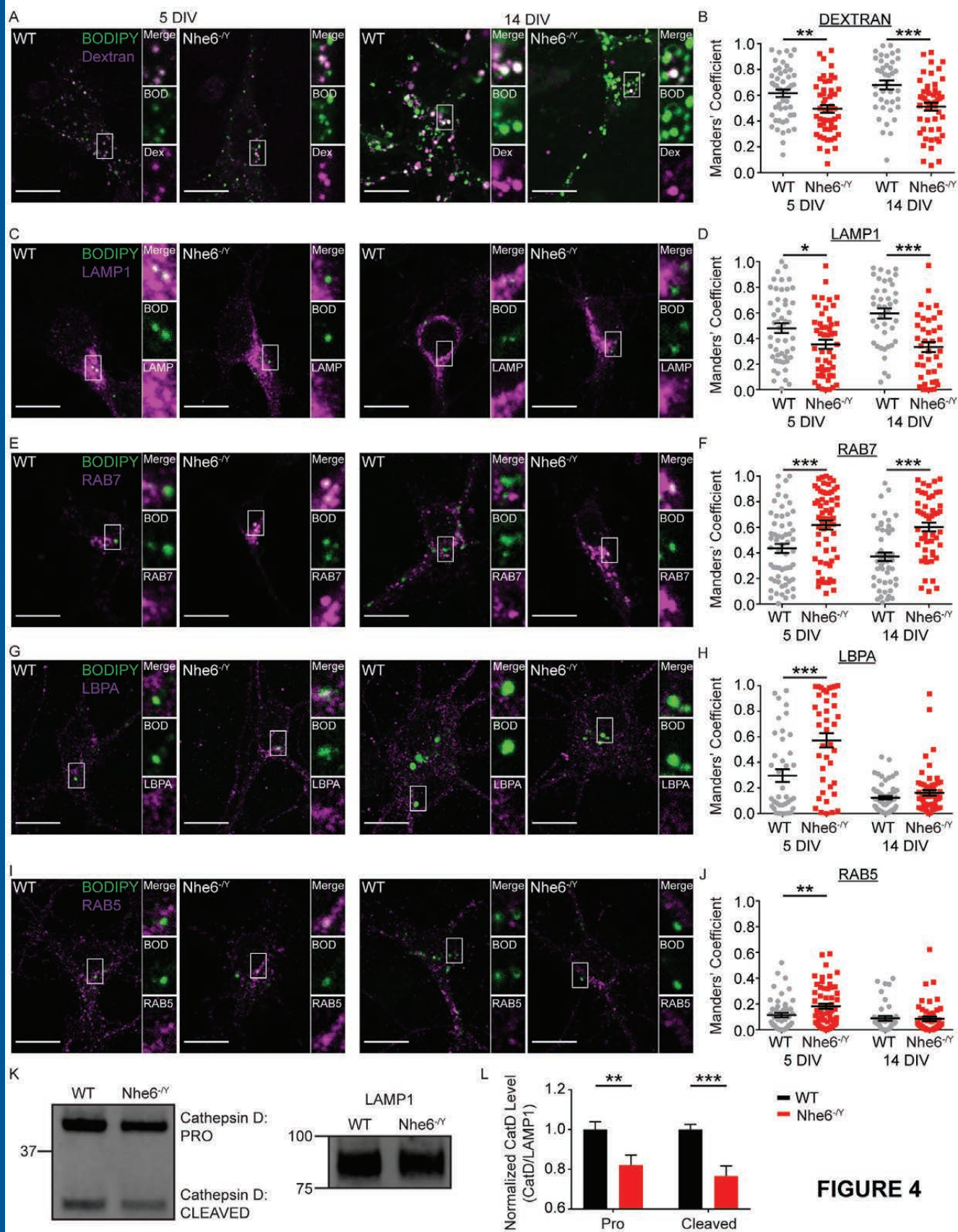


FIGURE 3



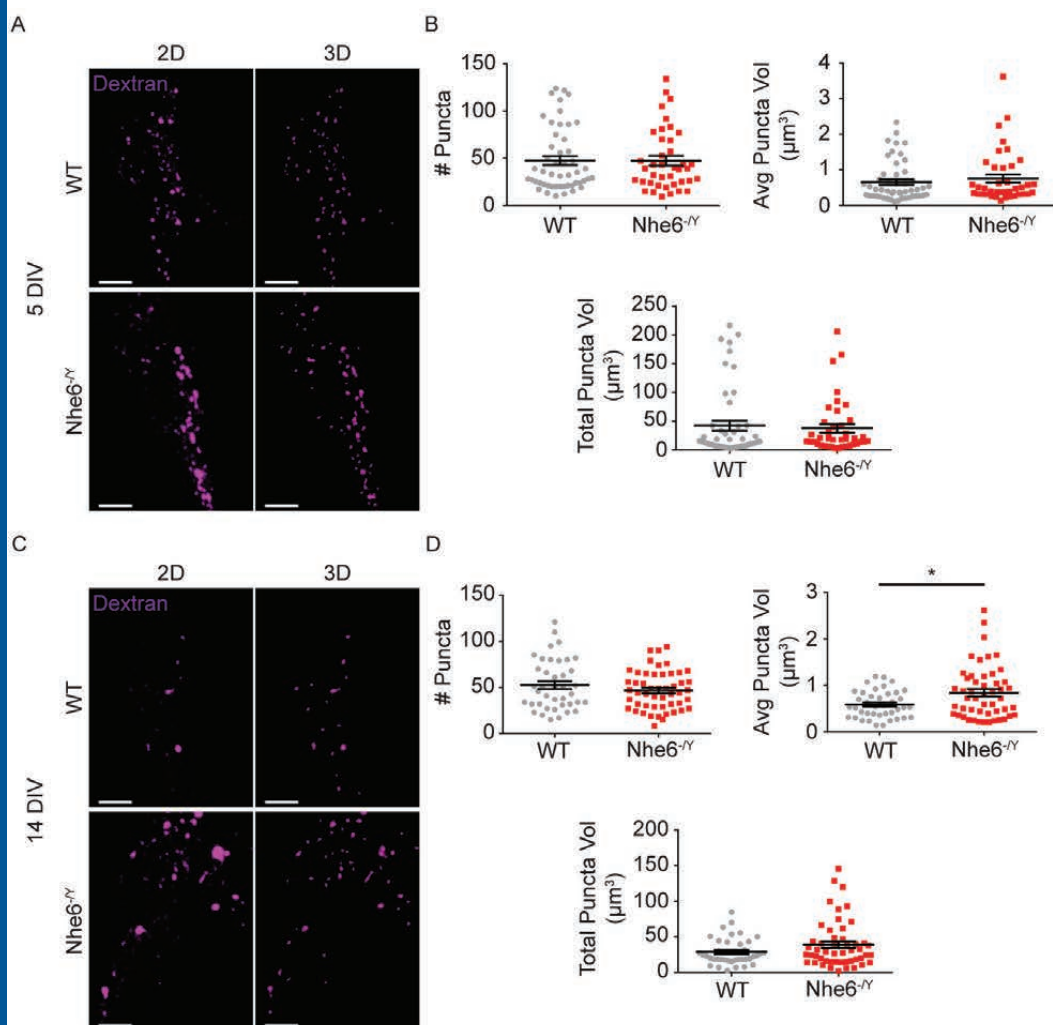


FIGURE 5

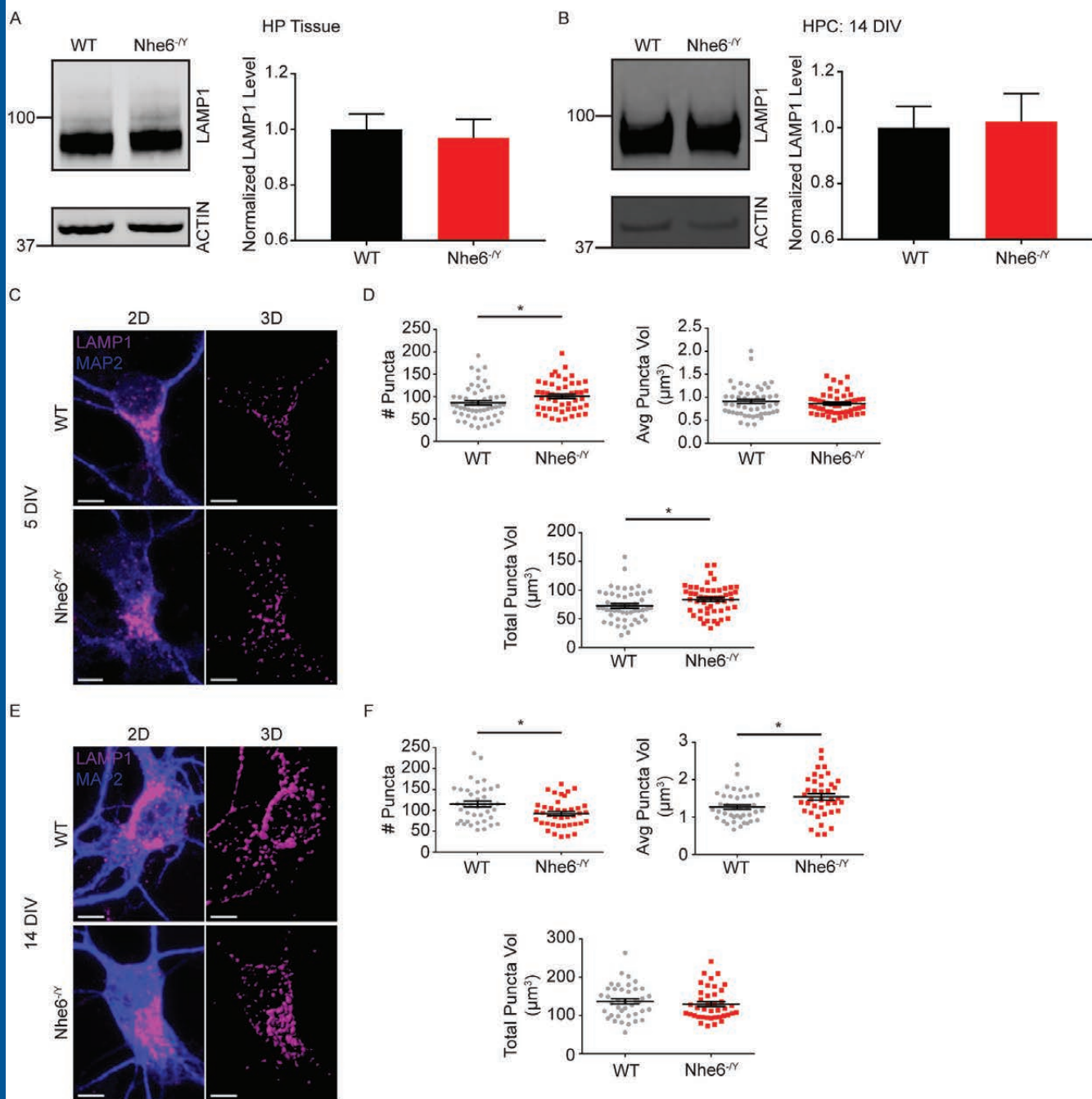


FIGURE 6

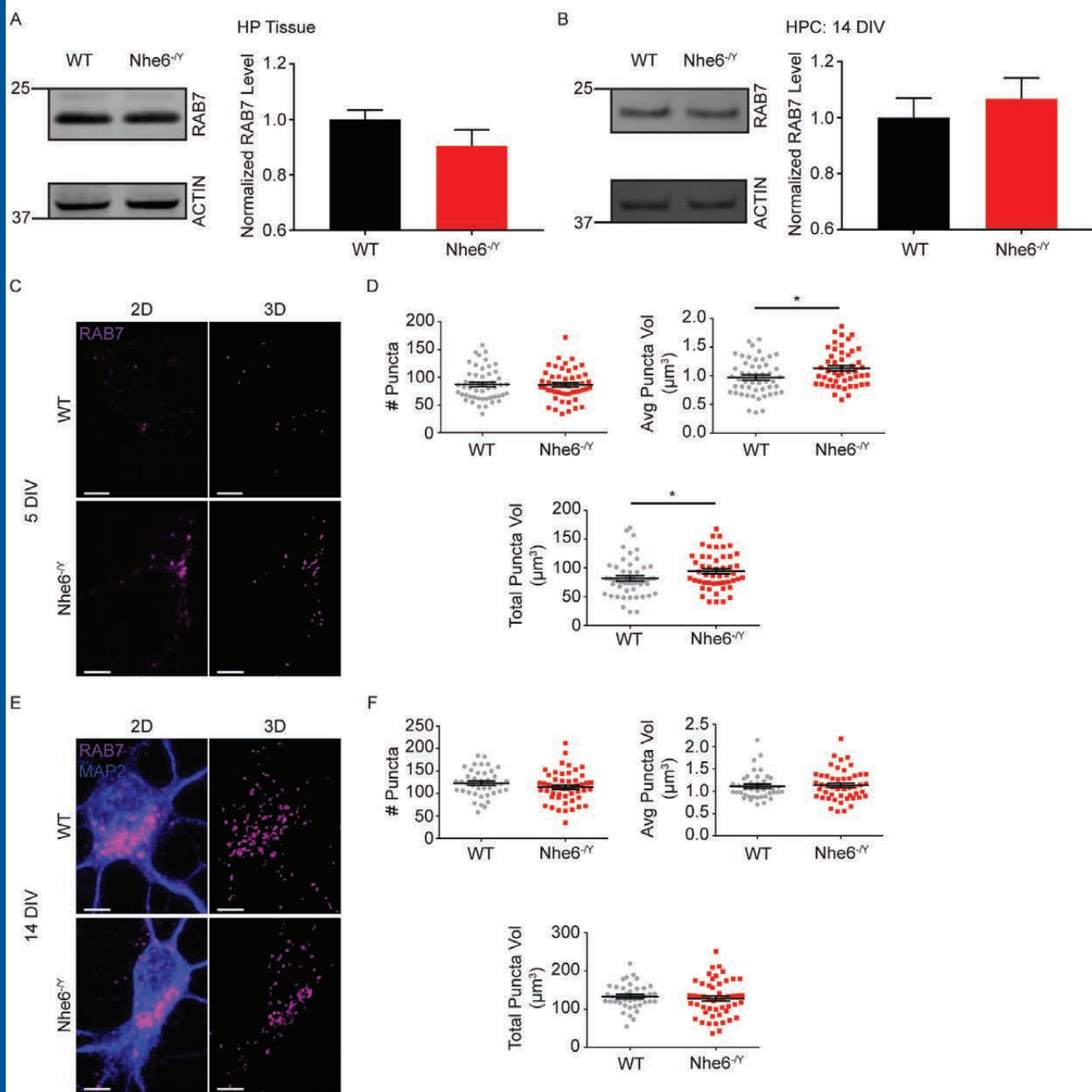


FIGURE 7

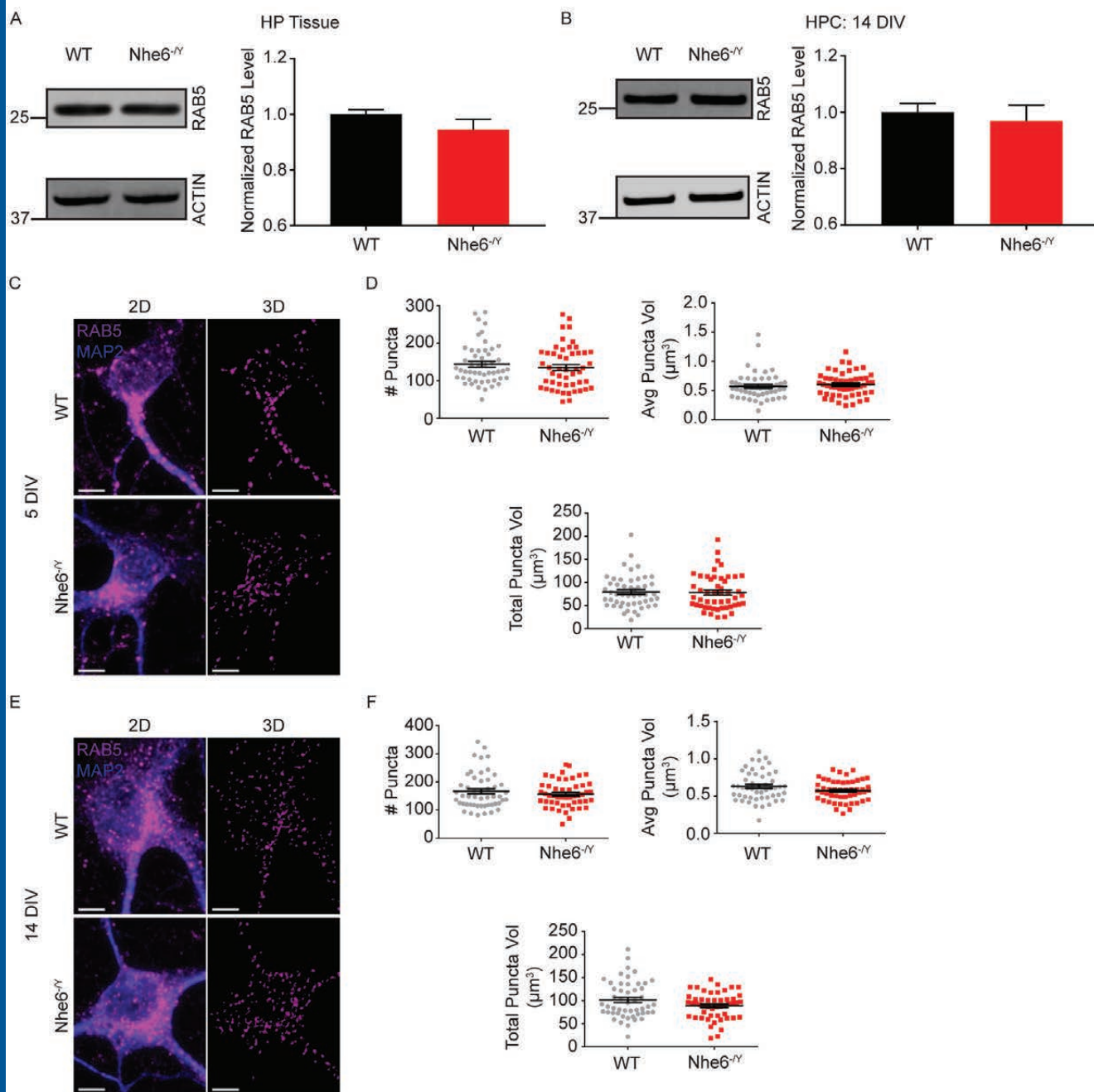


FIGURE 8

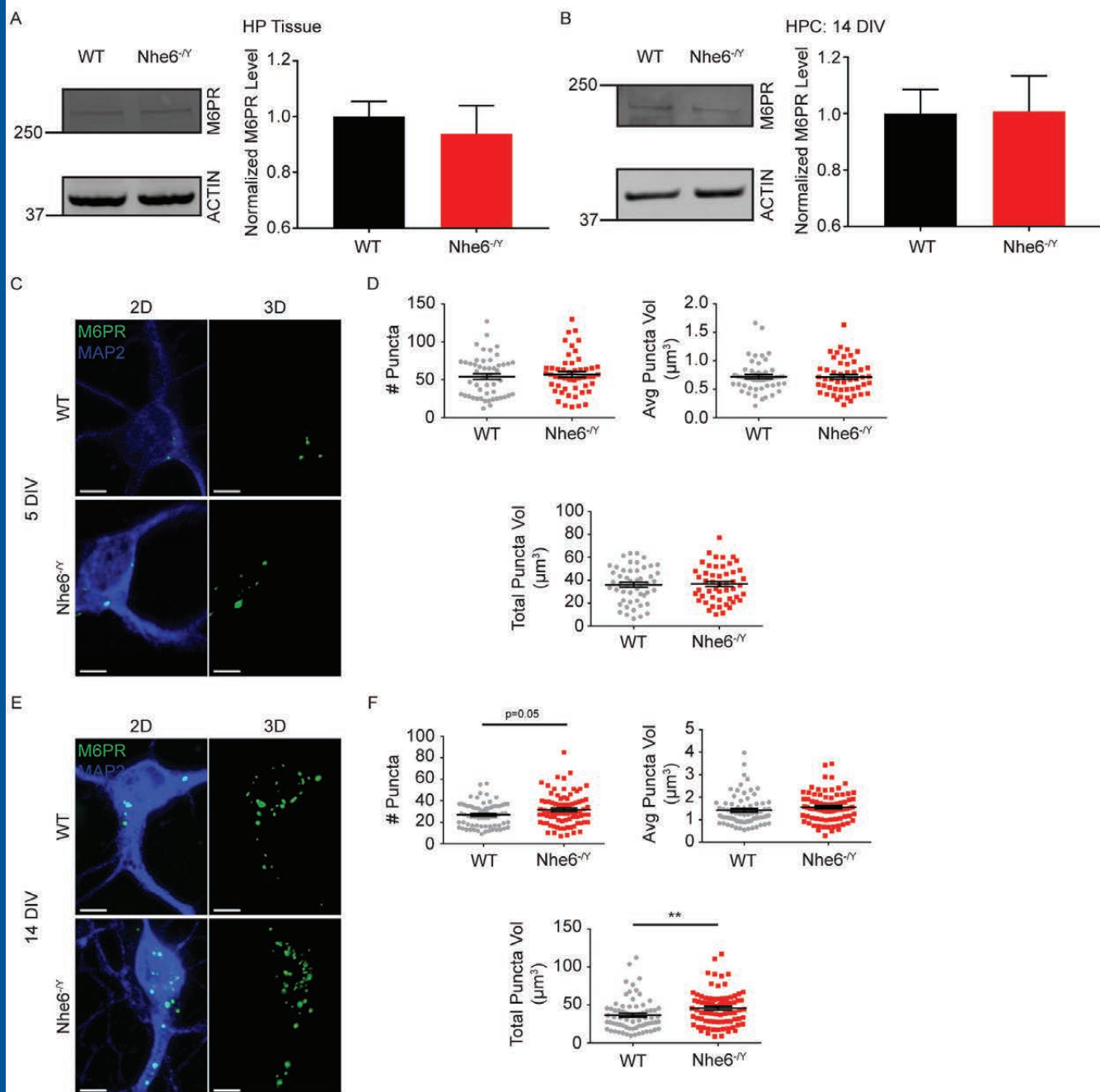


FIGURE 9

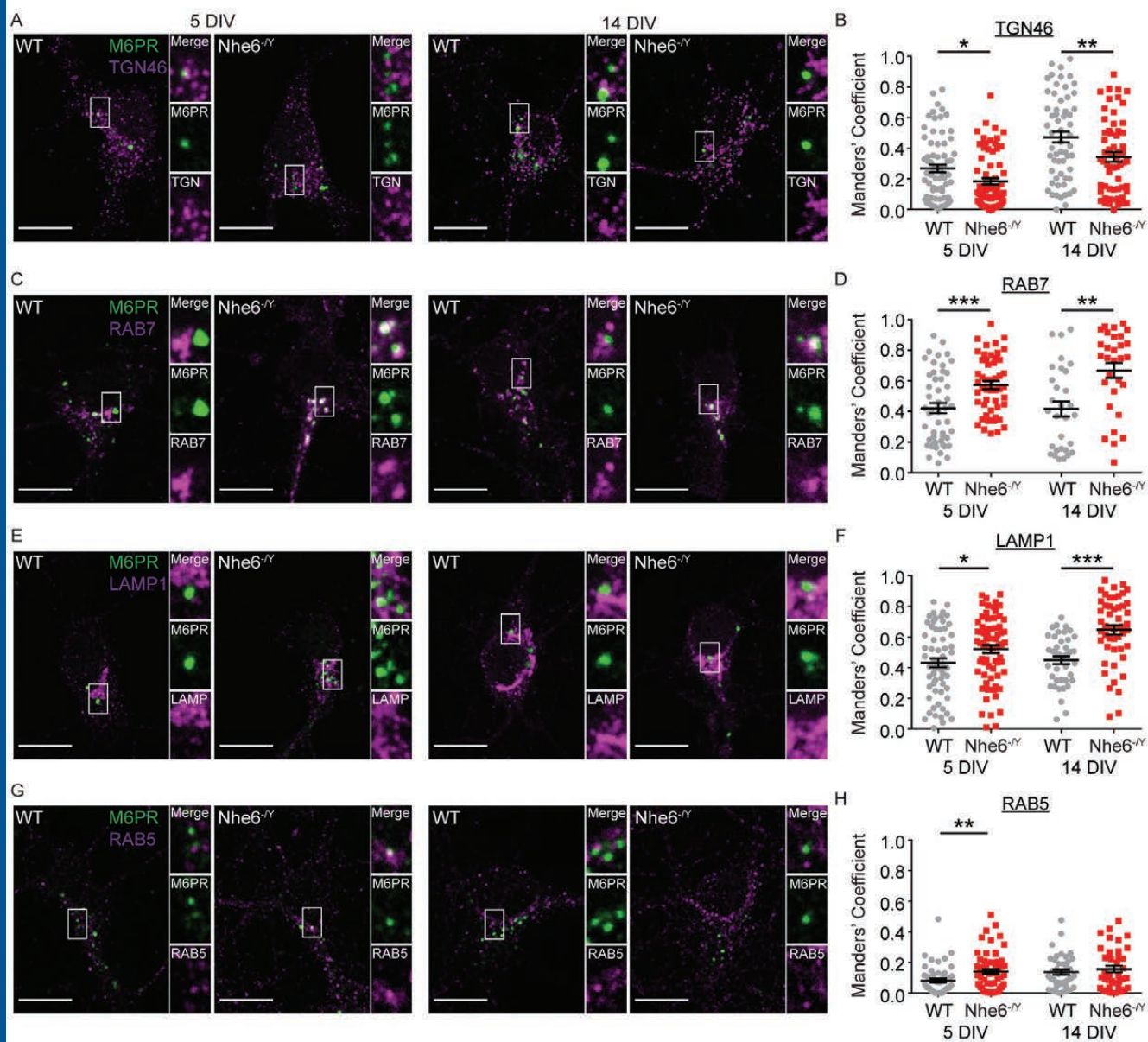


FIGURE 10

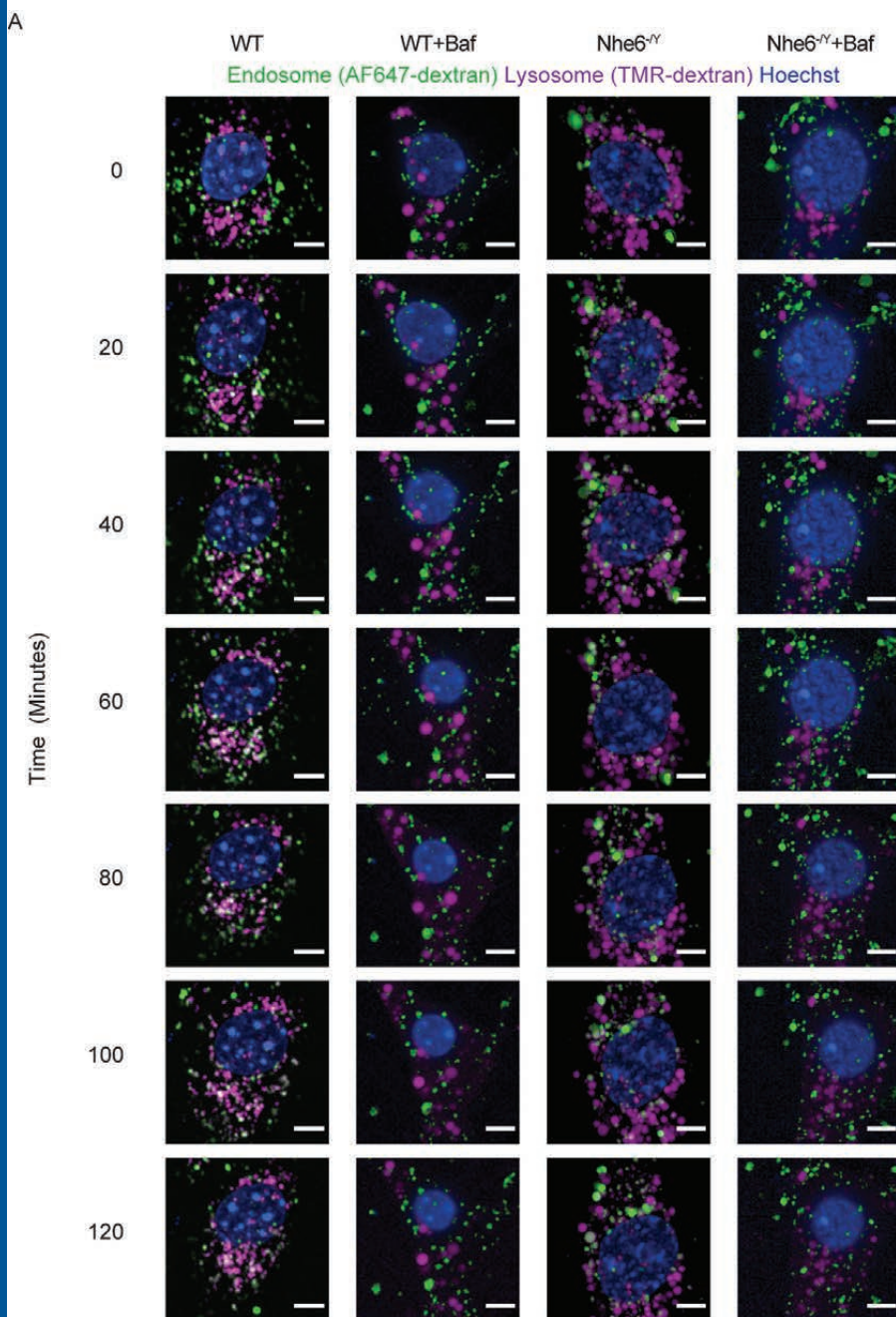
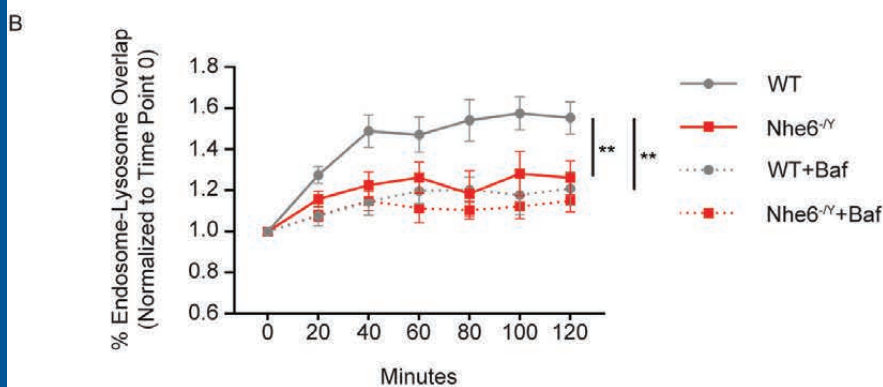


FIGURE 11



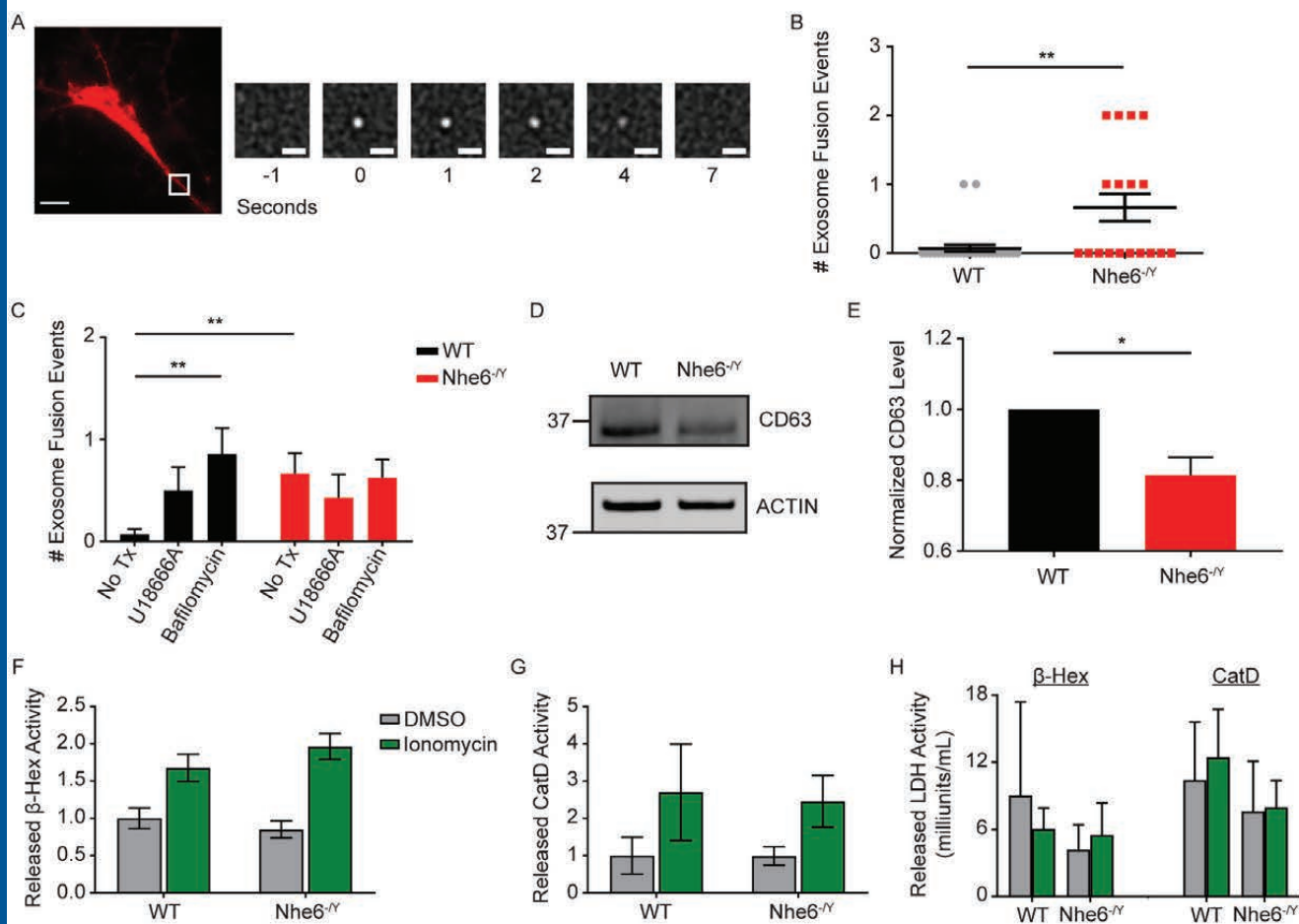


FIGURE 12

FIGURE 13

